Volume 33
DOE/DP40200-65

LLE Review

Quarterly Report

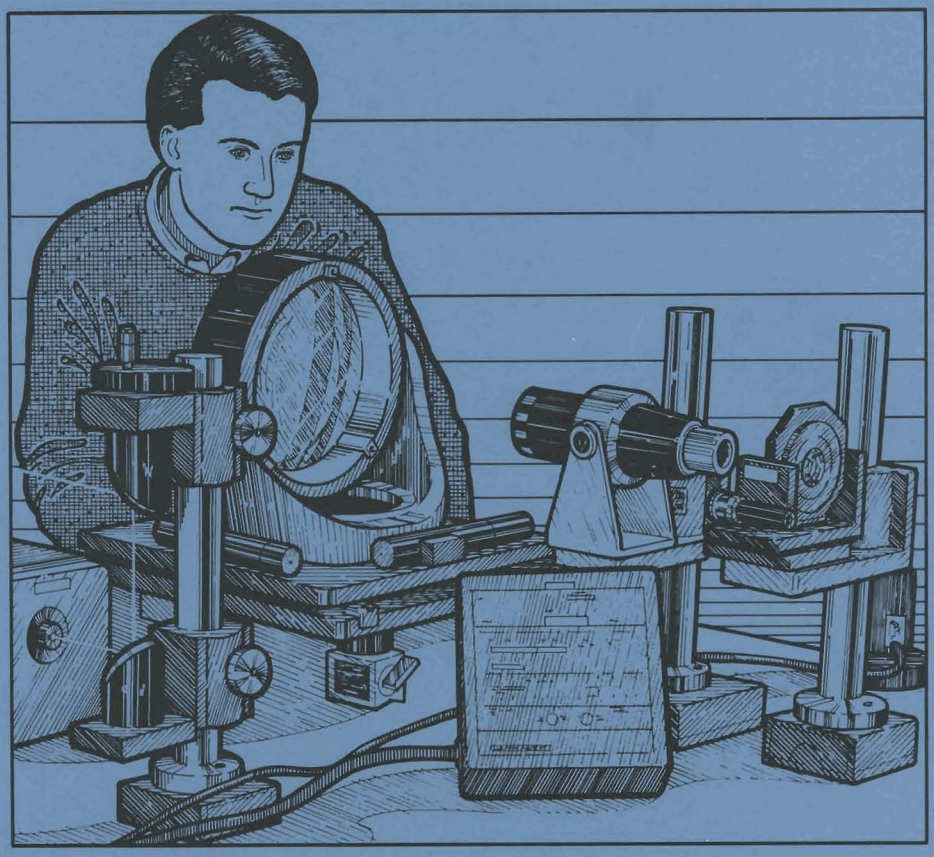

October–December 1987

Laboratory for Laser Energetics
College of Engineering and Applied Science
University of Rochester
250 East River Road
Rochester, New York 14623-1299

Volume 33
DOE/DP40200-65

LLE Review

Quarterly Report

Editor: J. Kelly
(716) 275-4710

October–December 1987

Laboratory for Laser Energetics
College of Engineering and Applied Science
University of Rochester
250 East River Road
Rochester, New York 14623-1299

IN BRIEF

This volume of the LLE Review, covering the period October–December 1987, contains descriptions of the implementation of distributed phase plates for improved irradiation uniformity and the implementation of a cryogenic target capability on the OMEGA facility. The section on advanced technology has reports on the design and optimization of recombination x-ray lasers and a near-infrared dichroic dye for use in both active and passive liquid-crystal devices. Finally, the activities of the National Laser Users Facility and the GDL and OMEGA laser facilities are summarized.

The highlights of this issue are

- Distributed phase plates, implemented on OMEGA, have made the target-plane illumination uniformity insensitive to near-field phase and intensity errors that previously produced hot spots on target.

- An integrated system for producing, positioning, protecting, and documenting microballoons containing a frozen DT layer was put into operation on the OMEGA target chamber.

- Recent modeling results using a new, explicit nonlocal treatment of the Doppler-enhanced escape probability of the resonance radiation has shown short-pulse illumination and cylindrical expansion to be very important for producing net gain in carbon recombination x-ray lasers.

- A near-infrared-absorbing, liquid-crystalline dye has been shown to exhibit dichroic behavior in nematic liquid-crystal hosts. This dye has superior optical absorbance in the 1-μm-wavelength region and excellent solubility in nematic hosts. These properties make this dye/host combination particularly interesting for device applications such as blocking filters, shutters, and modulators for the near infrared.

CONTENTS

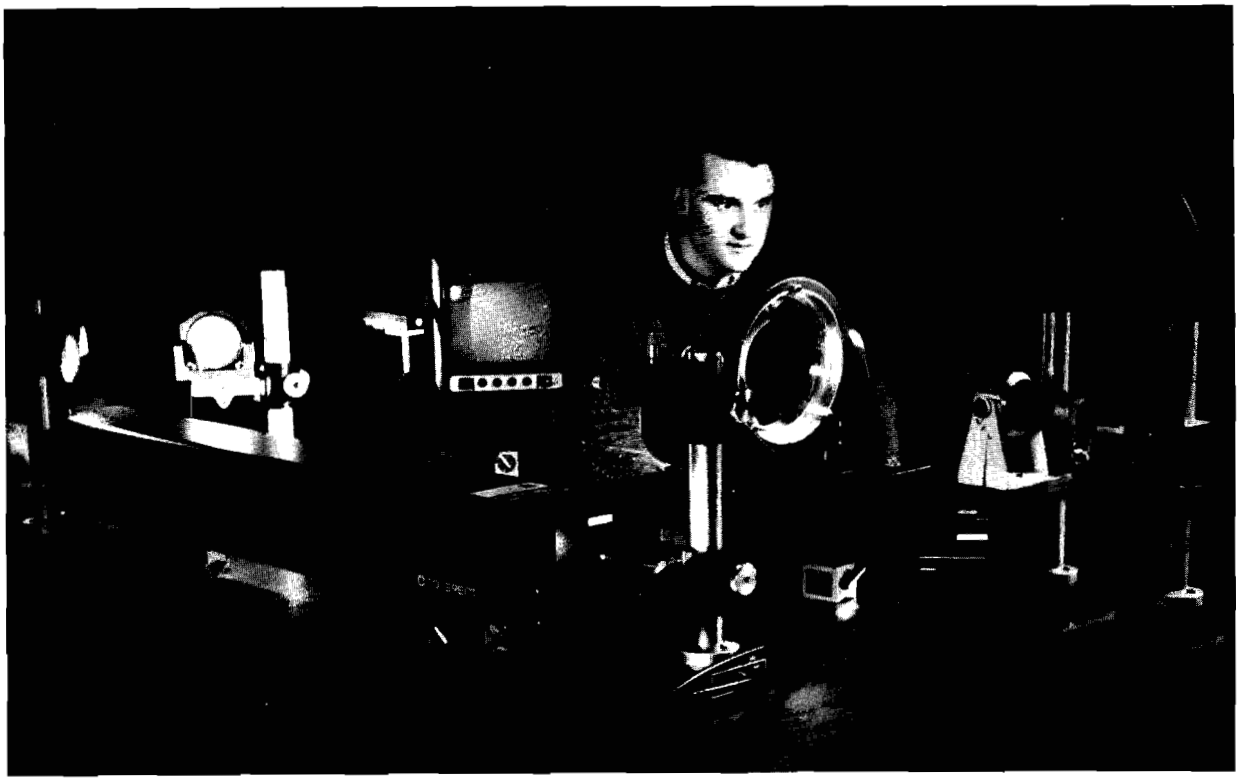

Phase conversion of the OMEGA laser system has increased the level of irradiation uniformity on target. William Castle, a member of the Optical Engineering Group, uses high-resolution interferometry to test distributed phase plates.

Section 1
PROGRESS IN LASER FUSION

1.A OMEGA Phase Conversion with Distributed Phase Plates

Introduction

An essential requirement for direct-drive laser fusion is the uniform irradiation of spherical targets that are located in the quasi far field of a laser system. Uniform absorption of laser light results in improved spherical convergence of the target during high-density compression. A major impediment to irradiation uniformity with high-power, solid-state laser systems is the presence of hot-spot structure, in each of the frequency-converted beams, at the target plane.[1]

The hot-spot intensity nonuniformities are caused by spatial variations in the near-field phase front of each laser beam. Although for many tabletop applications diffraction-limited laser performance can be obtained through static phase correction, adaptive optics, or phase conjugation, such approaches are either excessively expensive, difficult to implement, or not yet available for large-aperture, high-peak-power laser beams.

An alternative to phase correcting a wave front involves modifying the laser beam's coherence properties, thereby changing its focusing characteristics. The method of induced spatial incoherence[2] involves a reduction in both spatial and temporal coherence. This technique currently precludes third-harmonic generation and requires expensive apparatus. Other methods are based on modifications of only the spatial coherence of a laser beam.[3,4] In general, a beam is subdivided into many beamlets, each individually phase modified (converted), and

then recombined at the target plane, much like a multibeam far-field interferometer.

A phase-conversion technology that incorporates a distribution of near-field phases to either perform static phase correction or induce spatial incoherence offers a degree of flexibility needed at this stage of research. Distributed-phase-plate technology, recently deployed on the OMEGA laser system, offers this parallel route toward increasingly higher levels of irradiation uniformity.

Analytical Design

Classical physical optics provides an understanding of the far-field intensity control obtained through phase conversion. A distributed phase plate (DPP), schematically represented in Fig. 33.1, is composed of an ordered array of transparent hexagonal elements. Phase retardation is randomly distributed among the elements by introducing optical path differences (OPD) using a thin-film layer of thickness t and refractive index n_λ. The exact amount

$$\phi = \frac{2\pi}{\lambda}\,[\mathrm{OPD}] = \frac{2\pi}{\lambda}\,[t\,(n_\lambda - 1)] \qquad (1)$$

of phase retardation ϕ experienced by a transmitted wave front depends upon the wavelength λ of light.

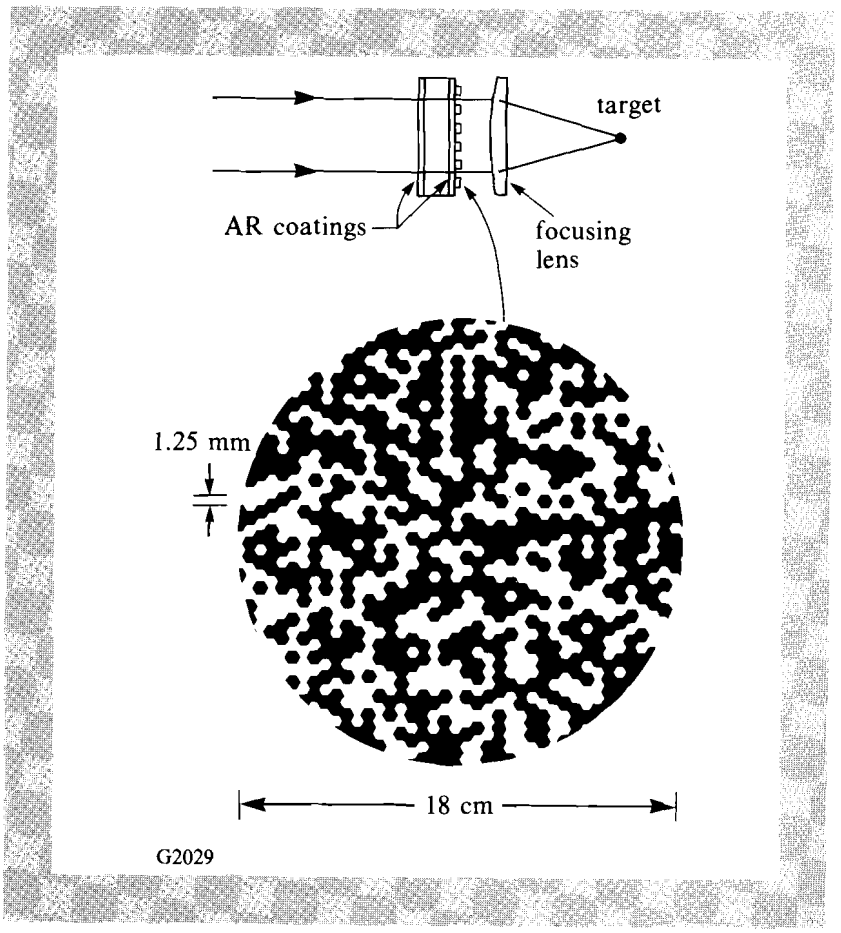

Fig. 33.1
Current distributed phase plates are composed of an ordered array of transparent elements. The phase values of approximately 15,000 hexagons are randomly binned into two levels that differ in phase by π radians. The diffraction patterns of the hexagonal beamlets are collected and brought to focus for target irradiation.

Collimated laser light is transmitted through the DPP, broken into coherent, phase-retarded beamlets, and brought to focus, where a superposition of beamlets is formed.[5] The amplitude distribution at the Fourier transform (focal) plane is given by

$$A\ (\epsilon,\eta) = \int_{-\infty}^{\infty}\int a\ (\alpha_1,\beta_1)\ e^{-2\pi i(\alpha_1\epsilon+\beta_1\eta)}\ d\alpha_1\ d\beta_1\ , \qquad (2)$$

where $a(\alpha_1, \beta_1)$ is the complex amplitude distribution and $\epsilon = \alpha_2/(\lambda f)$, $\eta = \beta_2/(\lambda f)$ are the spatial-frequency variables. The input amplitude is a product of the laser beam amplitude (denoted by the subscript L) and the amplitude transmittance of the DPP:

$$a\ (\alpha_1,\ \beta_1) = \Psi_L\ (\alpha_1,\ \beta_1) e^{i\phi_L\ (\alpha_1,\beta_1)} \cdot \sum_{j=1}^{N}\sum_{k=1}^{N} \mathrm{CIRC}\left[\frac{\sqrt{(\alpha_1-\alpha_j)^2 + (\beta_1-\beta_k)^2}}{d_o}\right] e^{i\phi_{R_{j,k}}}\ . \qquad (3)$$

The circle function (CIRC)[6], defined as

$$\mathrm{CIRC}\left[\frac{r}{d_o}\right] \equiv \begin{cases} 1 & o \le r < d_o/2 \\ 1/2 & r = d_o/2 \\ 0 & r > d_o/2 \end{cases} ,$$

closely approximates the hexagonal element. The random variable $\phi_{R_{j,k}}$ represents the phase retardation of the $(j,k)^{\text{th}}$ element. Substituting Eq. (3) into Eq. (2) yields

$$A\ (\epsilon,\eta) = \int_{-\infty}^{\infty}\int \Psi_L\ (\alpha_1,\ \beta_1)\ e^{i\phi_L\ (\alpha_1,\beta_1)} \sum_{j=1}^{N}\sum_{k=1}^{N} \mathrm{CIRC}\left[\frac{\sqrt{(\alpha_1-\alpha_j)^2 + (\beta_1-\beta_k)^2}}{d_o}\right] e^{i\phi_{R_{j,k}}}\ e^{-2\pi i(\alpha_1\epsilon+\beta_1\eta)}\ d\alpha_1\ d\beta_1\ . \qquad (4)$$

Since the transform of a product is equal to the convolution of the individual transforms, $A(\epsilon, \eta)$ can be more conveniently expressed as

$$A\ (\epsilon,\ \eta) \propto A_L\ (\epsilon,\ \eta) \otimes \left[\frac{2\ J_1(\pi d_o \omega)}{\pi d_o \omega} \sum_{j=1}^{N}\sum_{k=1}^{N} e^{2\pi i\left(\epsilon\alpha_j+\eta\beta_k+\frac{\phi_{R_{j,k}}}{2\pi}\right)}\right]. \qquad (5)$$

The above expression represents the convolution (denoted by $\otimes$) between the far-field amplitude distribution of the laser beam $A_L(\epsilon, \eta)$ and the product of a low-frequency envelope and a superposition of random spatial-frequency harmonics. This convolution is responsible for the detailed power spectrum of the resulting intensity distribution. The envelope, known as the Besinc function, where

$$\omega = \sqrt{\epsilon^2 + \eta^2}\ ,$$

represents the slowly varying profile of the focal intensity distribution $I(\epsilon, \eta)$:

$$I(\epsilon, \eta) = A(\epsilon, \eta)\, A^*(\epsilon, \eta) \propto \left[\frac{2J_1(\pi d_0 \omega)}{\pi d_0 \omega}\right]^2 \tag{6}$$

The shape of this function, the Airy pattern, is shown in Fig. 33.2(a).

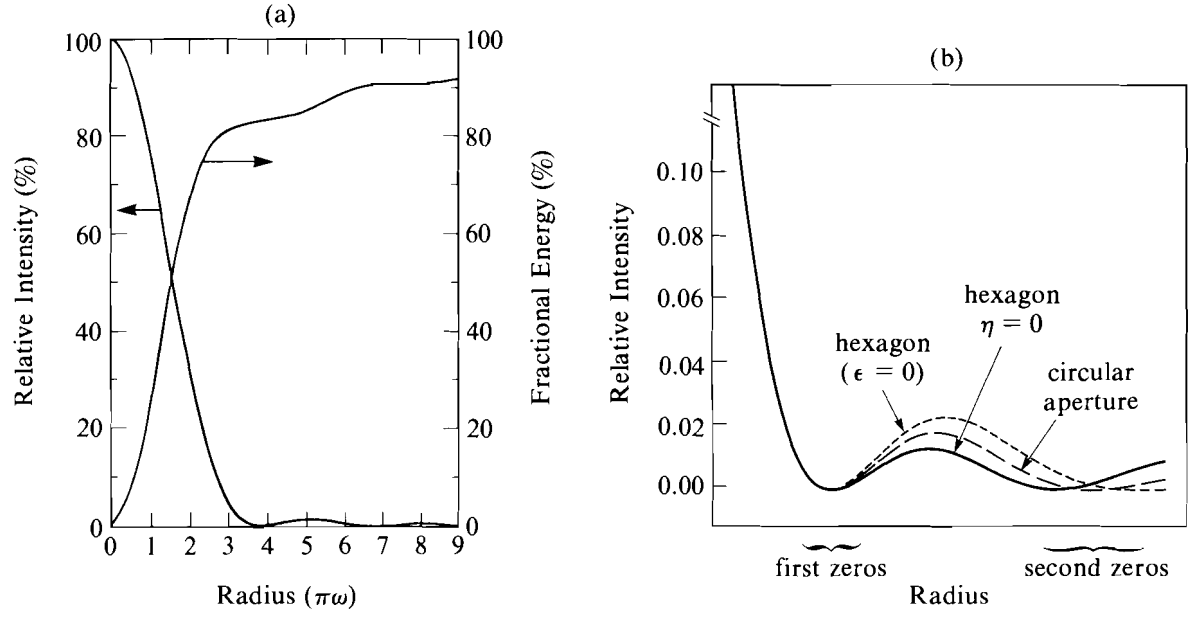

Fig. 33.2
(a) The encircled energy curve shows that more than 80% phase-conversion efficiency is obtained when the 5% intensity contour is tangentially mapped to the target. (b) The point-spread function (PSF) approximates the diffracted laser light, due to each hexagonal element, observed at the focal plane of a lens. The coherent addition of all the diffracted beamlets is also represented by a PSF envelope.

Since the actual diffraction structure is hexagonal and not circular, some justification for use of a circular aperture with an equivalent area is needed. Two major axes, along the lines of symmetry, define the profile of the hexagon Fourier transform. The transforms are given by

$$I(\epsilon, o) \propto \left[2\,\mathrm{sinc}(d\epsilon) + \mathrm{sinc}^2\left(\frac{d\epsilon}{2}\right)\right]^2 \tag{7}$$

and

$$I(o,\eta) \propto \left[4\,\mathrm{sinc}^2\left(\frac{d}{\sqrt{3}}\eta\right) - \mathrm{sinc}^2\left(\frac{d}{2\sqrt{3}}\eta\right)\right]^2, \tag{8}$$

where d is the hexagon width and $\mathrm{sinc}(x) \equiv \sin(\pi x)/(\pi x)$. Assuming equal areas, d and d_0 are related by $d_0 = (2\sqrt{3}/\pi)^{1/2}\, d$. Identical profiles, up to the first zero [as shown in Fig. 33.2(b)], validate modeling with a circular diffraction source of equivalent area.

From Eq. (6), and substitution of the spatial-frequency variable, the diameter of the first intensity zero is given by

$$D_{\mathrm{Airy}} = \frac{2.44\,\lambda f}{\left(\frac{2\sqrt{3}}{\pi}\right)^{1/2} d}, \tag{9}$$

where f is the lens focal length and λ is the wavelength of light. Equations (6) and (9) are used to design the DPP for a given target size and irradiation strategy. For the OMEGA laser, $\lambda = 0.351$ μm, $f = 593$ mm, and the target diameter is $D_T = 300$ μm. To obtain focusing with the 5.5% intensity contour at tangential focus, $D_{\text{Airy}} = 387$ μm, $d_o = 1.313$ mm, and $d = 1.250$ mm.

A simple relation determines the approximate number of hexagonal elements (N^2):

$$\left(\frac{D_{\text{Airy}}}{d_T}\right)^2 \sim \left(\frac{D_B}{d_o}\right)^2 = N^2 \sim 10{,}000 \ . \tag{10}$$

D_B is the beam diameter and d_T, the smallest intensity structure within the envelope, is approximately 1% of the target diameter.

The encircled fraction of energy[7] is given by

$$E_{\text{enc}}(\omega) = 1 - J_0^2(\pi d_o \omega) - J_1^2(\pi d_o \omega) \tag{11}$$

and is shown in Fig. 33.2(a). Table 33.I, showing the relative intensity and encircled energy as a function of target diameter, was generated from the plots in Fig. 33.2(a).

Table 33.I
Relative edge intensity and encircled energy versus target diameter.

Target Diameter (μm)	I/I_o(%)	E_{enc}(%)
280	9.1	79.5
290	7.2	80.6
300	5.5	81.5
310	4.2	82.2
320	2.9	82.8
387	0.0	83.8

G2232

DPP Fabrication and Testing

The fabrication procedure begins with the computer generation of an image containing a black-and-white version of the desired geometrical array of phase elements. Next, the fused-silica substrate is coated with antireflection coatings. The binary mask is transferred to the DPP glass substrate using photolithography. A positive photoresist layer is then spin deposited on one side of the substrate. After the resist layer is made more durable, through oven baking, it is exposed to ultraviolet radiation through the photographic mask. Chemical development of the photoresist produces a positive image of the photographic mask. A thorough cleaning process prepares the resist-mask substrate for the overcoat-deposition stage.

Following the production of the resist mask, a thin SiO_2 layer is vapor deposited over the same surface of the substrate. A subsequent

lift-off procedure removes the underlying resist, along with the SiO_2 overcoat that is in contact with the resist. The SiO_2 and antireflection interfaces remain intact, with a measured edge profile of <5-μm rms variation. These remaining SiO_2 hexagonal structures are the source of the π phase retardation.

As shown in Fig. 33.3, spectral measurement of the coating, before and after the overcoat deposition, is a sensitive method for measuring overcoat thickness. A 1% thickness reproducibility is routinely achieved. The OPD experienced by a transmitted wave front, however, is also dependent upon the refractive index [see Eq. (1)]. High-resolution interferometry has shown optical path variations, between plates, of about 1% to 2% of a $\lambda/2$ phase structure. Variations in the refractive index of the SiO_2 layer may account for this plate-to-plate OPD variability.

The phase retardation between two different levels on a DPP is accurately measured with laser interferometry. The DPP is inserted into one arm of a Twyman-Green interferometer, operating at the relevant wavelength of $\lambda = 0.351$ μm. Double-pass interference fringes are imaged onto a solid-state camera and the image captured with a frame grabber interfaced to an IBM PC-XT[8] computer. Image transfer to a SUN-3[9] provides the required complex Fourier transform capabilities to complete one-dimensional, spatial-synchronous phase detection (SSPD).[10] SSPD is performed, column by column, through the interface between the two elements of different phase. The calculated phase, averaged over a column, is plotted as a function of the column number. Since double-pass interferometry causes a $\lambda/2$ piston shift to appear as a wavelength shift, exactly one fringe shift indicates no phase error. A nearly perfect $\lambda/2$ piston shift is shown in Fig. 33.4. SSPD accuracy for piston measurement is approximately $\lambda/400$ for data of this quality. Fabrication accuracy of better than $\lambda/100$ has been demonstrated for the DPP's deployed on the OMEGA laser system.

OMEGA Implementation

The distributed phase plates are characterized off line with continuous-wave radiation of wavelength $\lambda = 0.351$ μm. In addition to phase measurement, plate transmission and far-field performance are both analyzed. DPP transmission typically results in $80\% \pm 1\%$ of the incident light reaching a 300-μm-diameter target placed at the focal plane. The intensity distribution exhibits the Airy pattern envelope and the high-modulation, high-frequency intensity variations, as predicted by the theoretical design of the DPP's. In addition, the overall focal distribution is found to be relatively insensitive to near-field phase and amplitude errors caused by, for example, atmospheric turbulence and beam obstructions.

Within the inner sleeves of each of the 24 focusing assemblies, ring adapters securely hold DPP's close to the focus lenses. This configuration provides several advantageous design features. Removal and reinsertion of all DPP's can be completed within a system shot cycle to accommodate optimum pointing of beams on target. In

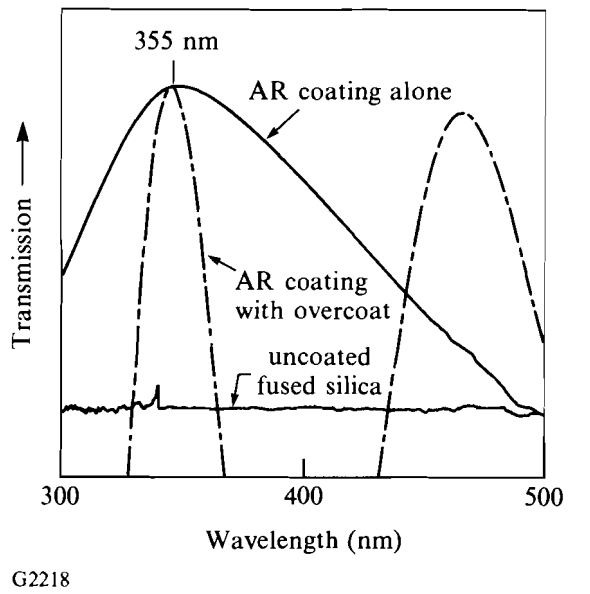

Fig. 33.3
The thin-film relief pattern is deposited over an antireflection coating. Spectral measurement of the coating, with and without an SiO_2 overcoat, is a sensitive method for determining the overcoat thickness. Optical path reproducibility of a few percent is limited by variations in the refractive index of SiO_2.

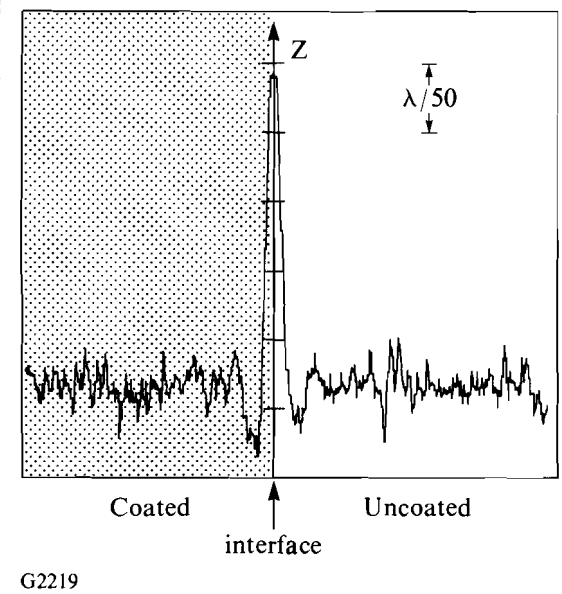

Fig. 33.4
The phase-retardance or optical-path difference between the two levels is accurately measured with laser interferometry. Spatial-synchronous phase detection is used to demonstrate better than λ/100 accuracy for a λ/2 hexagonal diffraction structure.

addition, the location near to the input side of the focus lens is relatively free of ghost radiation. Thin-film coating damage has not been observed. The OMEGA laser, barring laser component damage, can be operated at a fill factor that would normally degrade the uniformity on target. Therefore, the OMEGA laser system can be operated at higher uniformity and energy levels than were previously possible.

Equivalent-target-plane (ETP) intensity distributions are measured for beamline 6-2 of the OMEGA laser. Figure 33.5 shows the results for an ETP corresponding to a 300-μm-diameter target. DPP's provide a well-defined envelope, together with a power spectrum that is shifted to high spatial frequencies. Hot spots—of about 5%–10% of the target diameter—that are caused by near-field phase errors are replaced with fine speckle of about 1%–2% of the target diameter. Figure 33.6 quantifies the size and intensity of the hot spots and speckle.

Overall irradiation uniformity on target is assessed by computing a 24-beam superposition of intensities, followed by a spherical harmonic decomposition. Figure 33.7 compares the results for a typical OMEGA beamline, non-phase converted and phase converted. The rms (%) intensity nonuniformity is improved by a factor of 6 for modes $\ell = 2$

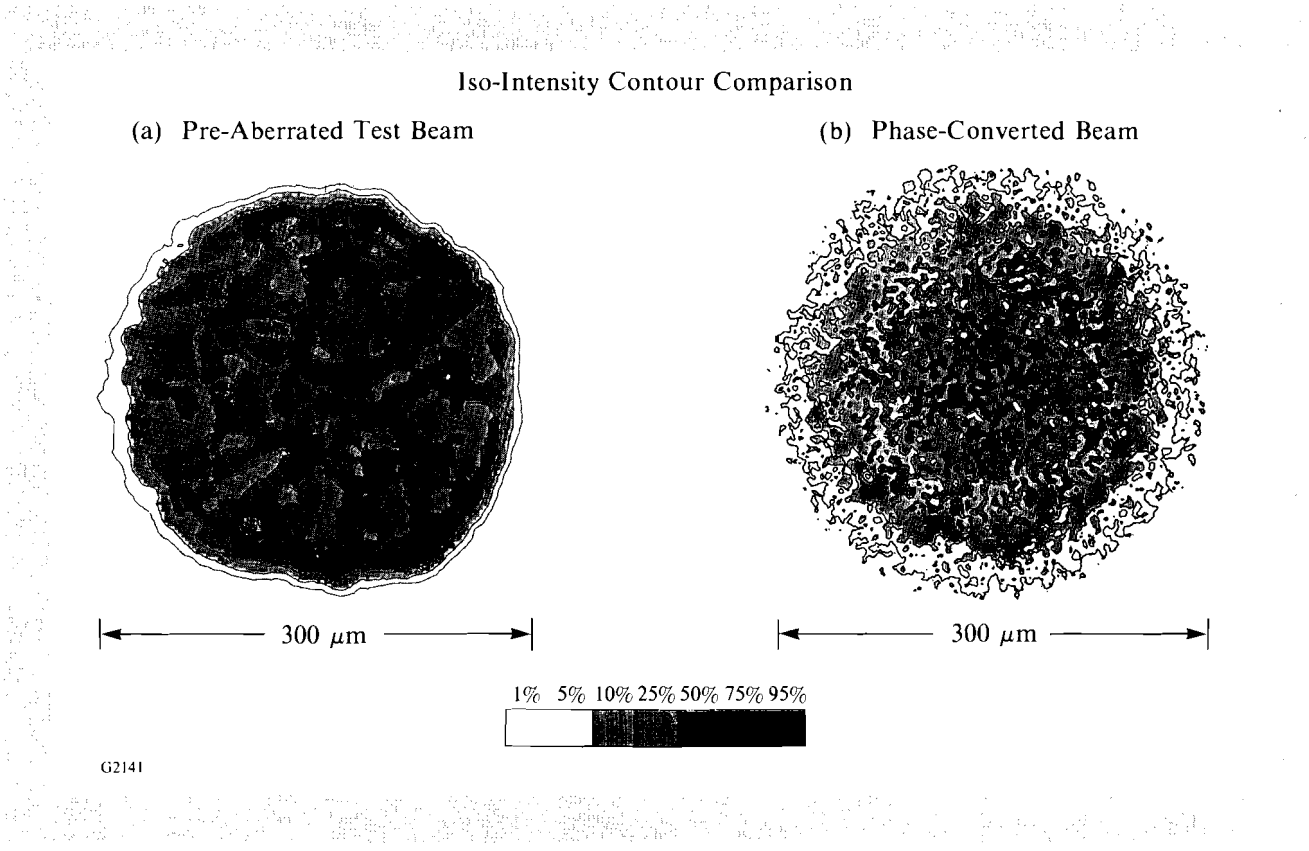

Fig. 33.5
Beamline 6-2 of the 24-beam OMEGA laser system is measured, before (a) and after (b) phase conversion, at an equivalent target plane of 300-μm diameter. Hot spots, caused by near-field phase errors, limit the uniformity levels on target. Distributed phase conversion produces a substantially different spatial-frequency spectrum, which is relatively insensitive to near-field phase errors.

through 20, and by a factor of 4 for modes $\ell = 2$ through 60. A smoothing of the beam by 1% of its diameter is assumed for this comparison.

A significant benefit of the DPP's is that they provide reproducible irradiation uniformity, which eliminates a major source of experimental compromise. Such reproducibility can be obtained with the OMEGA laser without DPP's only if atmospheric turbulence, beam misalignment, and accumulated birefringence are substantially reduced.

Applications

An essential requirement of direct-drive, inertial confinement fusion is the uniform irradiation of spherical targets that are placed in the quasi far field of a laser beam. Distributed phase plates provide substantially improved uniformity levels for targets placed close to the far-field plane. In addition to this primary goal, a variety of applications exists for this class of optical elements. As an example, the cylindrical focusing of laser light for x-ray laser target irradiation could include a DPP, since the narrow dimension of such targets is generally one to two orders of magnitude greater than the diffraction limit.

Further progress in distributed phase technology is anticipated. Higher levels of uniformity are expected with either N-level ($N \geq 3$) phase plates[11,12] or plate geometries that produce supergaussian

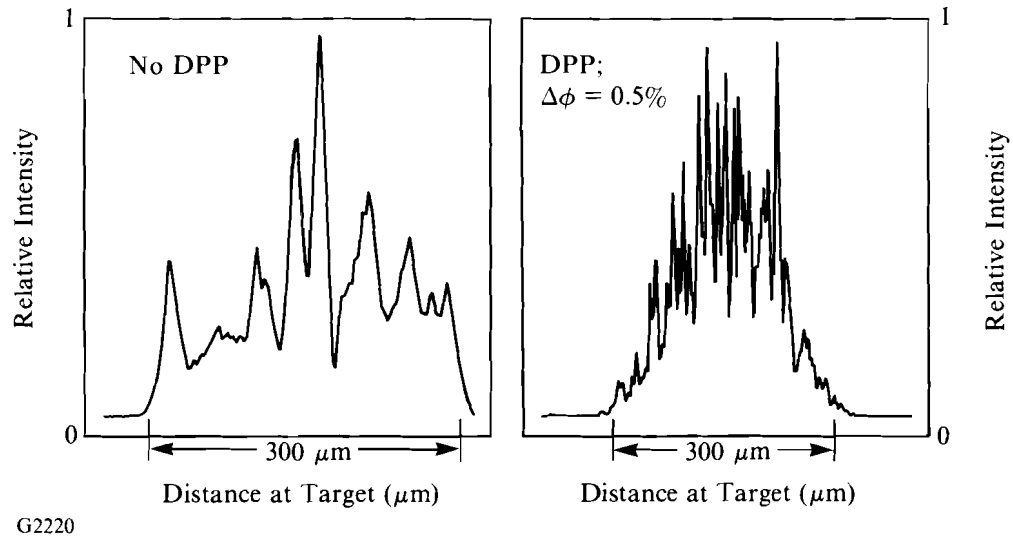

Fig. 33.6
Cross sections of the target-plane intensity distributions in Fig. 33.5 show, quantitatively, the differences before and after phase conversion. Numerous hot spots, each about 5%–10% of the target-plane beam diameter, are replaced by a reproducible and uniform envelope that contains small-scale speckle.

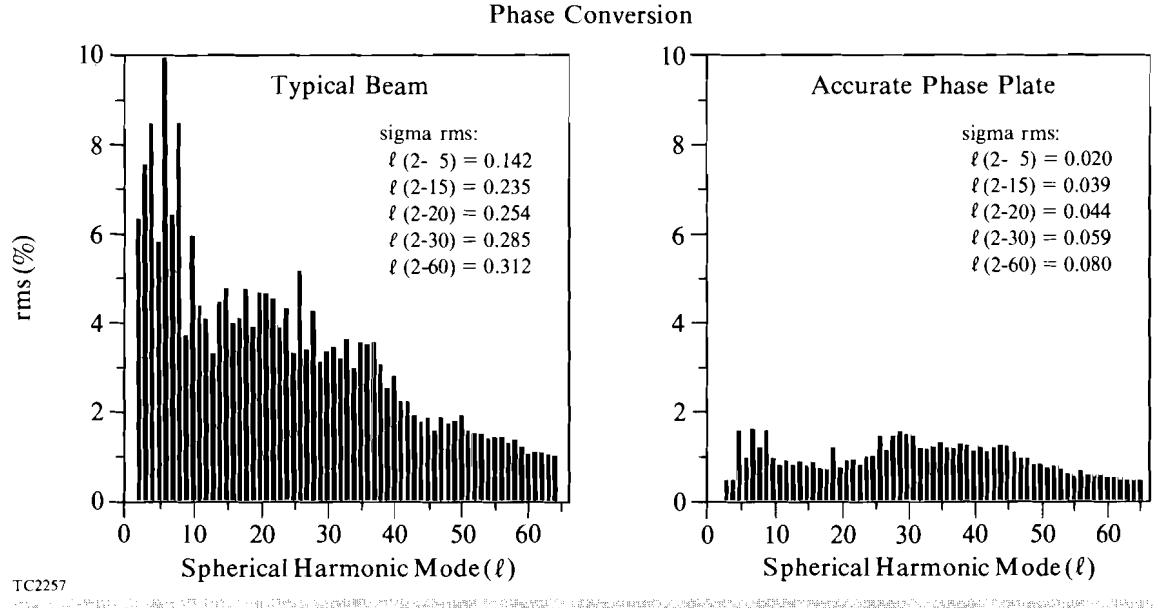

Fig. 33.7
Overall improvement of the irradiation uniformity on target is assessed by computing a 24-beam superposition of intensities and a spherical harmonic decomposition. The rms (%) intensity nonuniformity is improved by a factor of 6 for modes ℓ = 2 through 20, and by a factor of 4 for modes ℓ = 2 through 60. Smoothing by 1% of the beam diameter is assumed.

intensity profiles. Multiwavelength devices are also feasible. Furthermore, the DPP technology is a candidate for high-damage-threshold diffraction gratings.

Conclusion

The joining of many diverse technologies has resulted in the design, fabrication, and testing of high-quality distributed phase plates. Computerized image generation, photolithography, chemical vapor deposition, and high-resolution interferometry have been combined to make OMEGA the only frequency-tripled and phase-converted laser system. DPP's have improved the irradiation uniformity at the target plane by more than a factor of 3. In addition, the increased reproducibility of the beam profiles offered by the DPP's has made possible more critical assessment of shot-to-shot variations in beam energy balance and beam pointing. Other applications for distributed phase technology are anticipated.

ACKNOWLEDGMENT

This work was supported by the U.S. Department of Energy Office of Inertial Fusion under agreement No. DE-FC08-85DP40200.

REFERENCES

1. S. Skupsky and T. Kessler, *Phys. Rev.* (submitted for publication).
2. R. H. Lehmberg, A. J. Schmitt, and S. E. Bodner, *J. Appl. Phys.* **62**, 2680 (1987).
3. X. Deng *et al.*, *Appl. Opt.* **25**, 377 (1986).
4. Y. Kato *et al.*, *Phys. Rev. Lett.* **53**, 1057 (1984).
5. C. B. Burckhardt, *Appl. Opt.* **9**, 695 (1970).
6. J. D. Gaskill, *Linear Systems, Fourier Transforms, and Optics* (Wiley, New York, 1987), pp. 66–77.
7. M. Born and E. Wolf, *Principles of Optics*, 6th corrected ed. (Pergamon Press, New York, 1980), pp. 395–398.
8. PC-XT is a trademark of IBM, P.O. Box 1328-S, Boca Raton, FL 33432.
9. SUN is a trademark of SUN Microsystems, Inc., 2550 Garcia Avenue, Mountain View, CA 94043.
10. LLE Review **31**, 114 (1987).
11. W. C. Stewart, A. H. Firester, and E. C. Fox, *Appl. Opt.* **1**, 604 (1972).
12. Y. Takeda, Y. Oshida, and Y. Miyamura, *Appl. Opt.* **11**, 818 (1972).

1.B An Advanced Cryogenic Target-Positioning System

The past quarter has seen the completion of a difficult, multiyear project to provide a cryogenic (cryo) target capability for the OMEGA 24-beam irradiation facility.

Originally conceived in mid-1984, this project was to provide LLE with a cryogenic laser-fusion target capability based on the fast-refreeze technique pioneered by KMS Fusion[1] several years earlier at their own facility. The original plan was for KMS to develop a prototype system on a simulation chamber, which would be used to train LLE personnel in the operation of a cryo-target system and which then would be followed by a full system on the OMEGA tank. The simulation system, which was based on the old LLE ZETA tank, arrived at LLE in September 1986. A training session with KMS personnel followed after which it was decided to proceed directly to

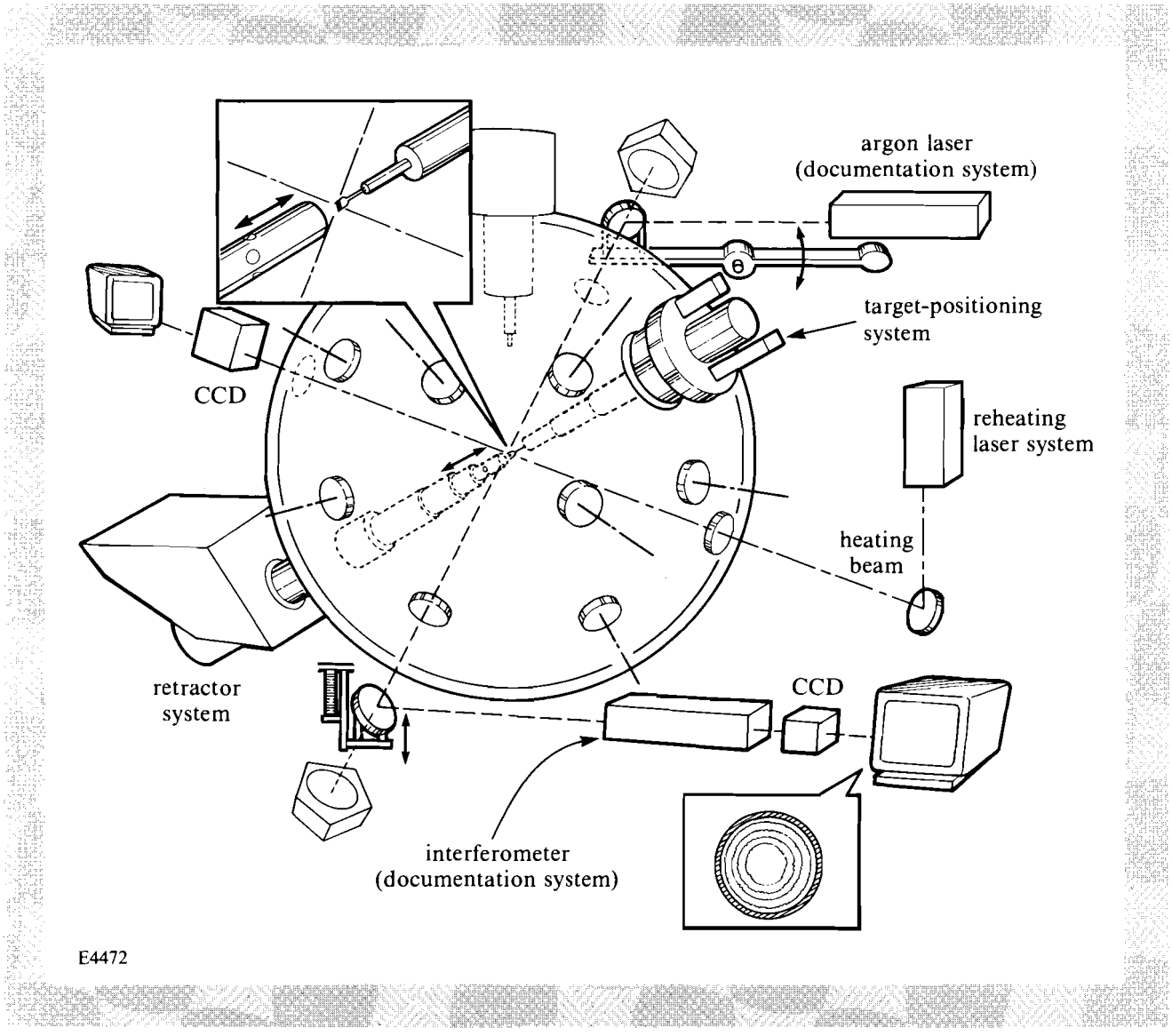

Fig. 33.8
Cryo-target subsystems on OMEGA.

the OMEGA implementation, using as much of the ZETA simulation hardware as possible. Interface hardware arrived from KMS in April 1987, and by mid-June the complete cryo system had been installed on the OMEGA tank. A number of laser shots were taken on cryo targets during the summer and early fall before it was decided to suspend cryo operations to perform a number of redesign activities. These activities substantially improved performance, and, as of this writing, more laser shots on cryogenically cooled targets are occurring. The ultimate goal is to compress a frozen pellet of DT ice to a final density of 100 times liquid hydrogen density.

There are four main parts of the cryo system. They are (1) the liquid-helium-cooled target-positioning stage; (2) the liquid-helium-cooled shroud and shroud-retractor system; (3) the reheating system; and (4) the documentation system. These subsystems are shown in Fig. 33.8 as they are arrayed on the OMEGA tank. The heart of the system is the He-cooled shroud and shroud-retraction system. In operation, the shroud, which is cooled to 16°K by liquid helium flowing through a cryostat, is also filled with cold helium gas bled off the cryostat. This cold gas is swirled around inside the shroud and around the target, refrigerating it and freezing the gas fill on the inside wall of the target balloon. The shroud, containing a stalk-mounted target, is shown in Fig. 33.9. This figure also shows the four sapphire windows inset into the gold-plated, solid-copper shroud. These four windows are for the documentation system and the heating-laser system, which will be described later. The purpose of the shroud-retraction system is to rapidly retract the shroud from around the target and leave an unobstructed path for the 24 main laser beams to be focused onto the target. Calculations and measurements of the lifetime of a solid layer of DT ice on the inside wall of a glass microballoon exposed to room temperature radiation yield times around 10 ms.[2] After 10 ms, a sufficient amount of fuel has melted and vaporized to significantly

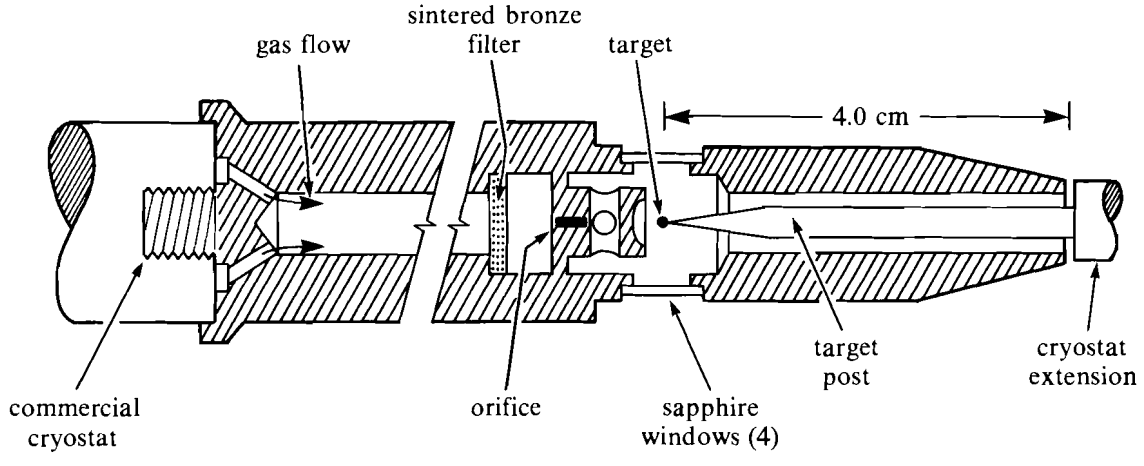

Fig. 33.9
Helium-gas shroud surrounding a cryo target.

affect the uniformity of the rest of the frozen fuel layer. In order to ensure a reasonably uniform frozen layer, exposure times—that is, the time between when the target first exits from the gas-filled shroud and the time at which the laser is fired on the target—should be much less than 10 ms. The original shroud-retraction system designed and supplied by KMS (see Fig. 33.10) used a vacuum bellows and electromagnetic release to provide the motive force for retracting the shroud. This system proved to be unreliable because the timing of the system was dependent upon the residual magnetism in the release electromagnet and was therefore prone to failure by early release.

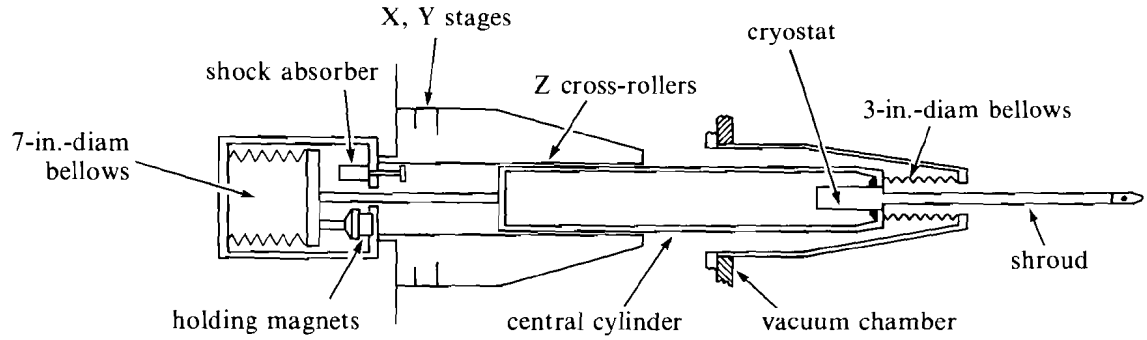

Fig. 33.10
Original shroud-retraction system showing shroud, cryostat, alignment stages, and retract mechanism.

The other major cryogenic component is the liquid-helium-cooled target positioner. While the target is cooled primarily by the cold gas from the cryo shroud mounted on the retractor, it is necessary to provide some cooling for the target mount. Because the shroud surrounds the target completely (with the exception of the four sapphire windows used for the documentation and heating systems), there is no way to view the target in two orthogonal directions for the purpose of alignment. Therefore, it was decided to align the target outside the shroud and ensure that no target motion could be induced by placing the shroud over the target. This necessitated cooling the target mount to almost the same temperature as the shroud so that all thermal contraction would have taken place before the shroud was inserted over the target.

The target positioner is unique in that it allows changing of targets between shots without breaking target-chamber vacuum. The target must be in good thermal contact with its cryostat, however, so the entire target positioner cryostat must be removed between shots. This is shown schematically in Fig. 33.11

The heart of this system is a ball-valve assembly, shown in Fig. 33.12, on the end of the re-entrant target positioner, which separates the separately pumped air lock from the main target chamber. An auxiliary vacuum system can evacuate the air lock to <1 mTorr in less than 10 min, much less than the proposed intershot time of 30 to

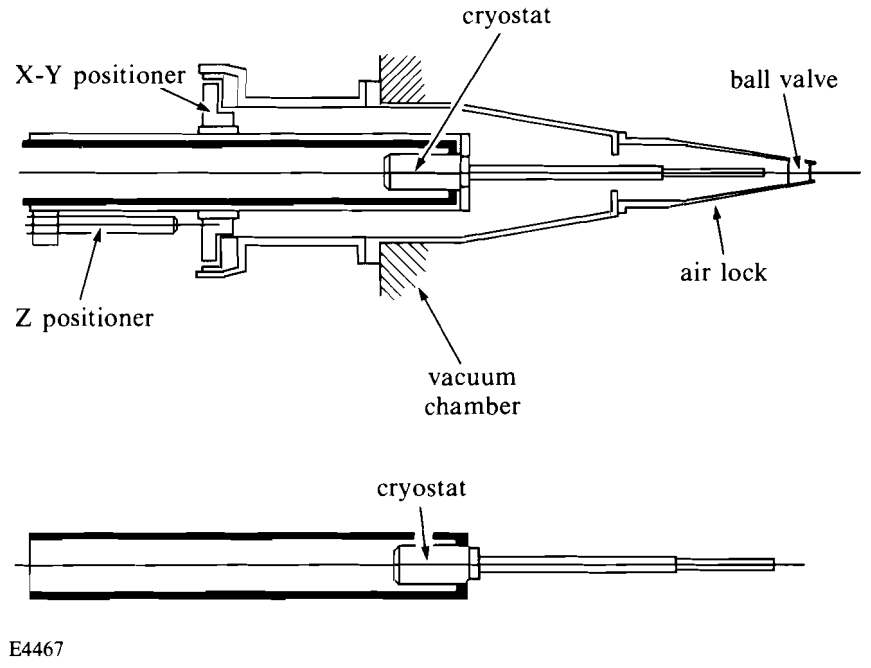

Fig. 33.11
Target-positioning system with cryostat; *X*, *Y*, *Z* stages; air lock; and ball-valve assembly.

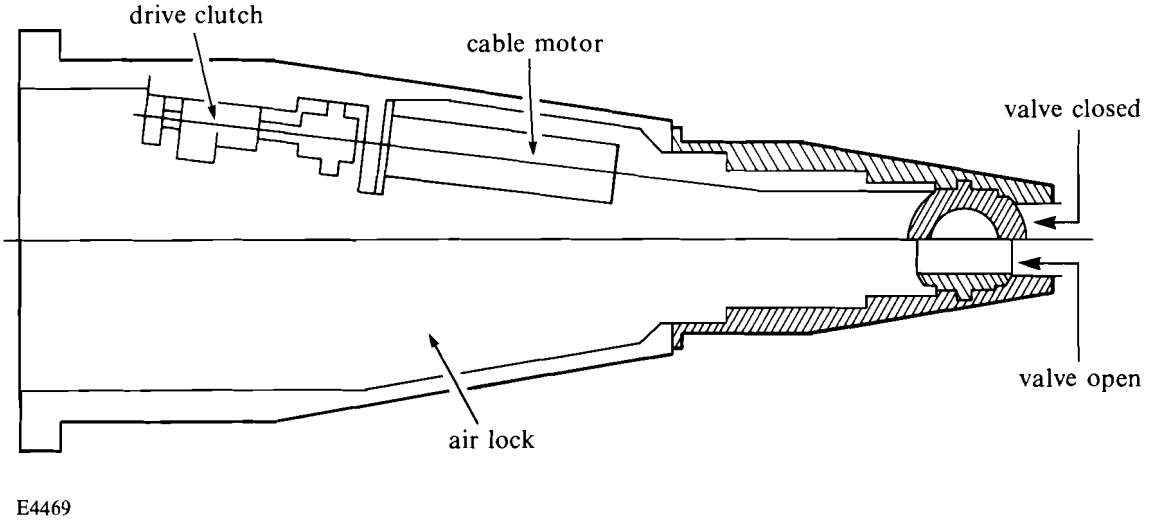

Fig. 33.12
Motor-driven ball-valve assembly, which allows interchanging targets without breaking target chamber vacuum.

45 min. The target positioning itself is done with a conventional three-axis positioning system, using computer-controlled microstepping motors to provide three uncoupled orthogonal axes of motion with 1-μm resolution and stability.

The other two major subsystems connected to the cryo-target system are the heating system and the documentation system. The heating system is a major component of the fast refreeze technique employed in this method of producing a uniform, frozen layer of DT ice on the inside wall of the target capsule. As the temperature of the microballoon is lowered slowly, the DT gas first liquefies, then forms a droplet that wets the inside wall of the balloon, and then, under the force of gravity, sags to the bottom of the balloon, where it freezes. However, if there is enough refrigeration power available to freeze the total mass of the gas on a time scale shorter than gravitationally induced sag, a uniform layer can be produced. The heating laser system attempts to do this. By focusing several watts of ultraviolet light from an argon-ion laser onto the target, it instantly evaporates the randomly frozen DT ice layer. If sufficient refrigeration is available, the ice layer will reform in a time short enough to preclude any gravitational sag and will produce a uniform, frozen layer. The purpose of the documentation system is to assure that a sufficiently uniform layer is produced.

The documentation system consists of a laser illuminator, an imaging system, an interferometer, and some method of recording and viewing the resulting interferogram. The block diagram for this system is shown in Fig. 33.13. This is a shearing-cube interferometer similar in design to the one originally used by KMS[3] but adapted to work at the longer distances imposed by the OMEGA tank dimensions. In the case of OMEGA, two opposing focusing lenses are used to illuminate the target and to image the target into the shearing cube. This means that flip-in mirrors must be used to first direct the light from the laser to the interferometer; then, a few seconds before the main laser is to be fired—after it is assured that the layer is going to remain frozen—these mirrors must retract out of the way of the main laser beams.

One of the major problems encountered during this project was the design of a nearly massless target mount. The KMS design of the gas shroud was based on the use of cylindrically symmetric stalk-mounted targets. In KMS experiments, carried out on CHROMA, the targets were mounted on thick glass or metal stalks.[4] To achieve the highest possible target performance, a very low mass target mount was needed. It was therefore decided to use a target mount that suspended a target on two or more short lengths of spider silk. Several early designs showed promise. The easiest to fabricate was a U-shaped piece of thin wire glued to a glass stalk, with spider silks stretched across the open top of the *U* and the target mounted in the center of the *U*. This worked well in tests of the shroud-retractor system, without cooling, but when the cold helium gas was allowed to cool the stalk and wire assembly, differential thermal contraction caused the assembly to twist and move the target out of the desired targeting point. Several attempts at isothermal designs were tried until the

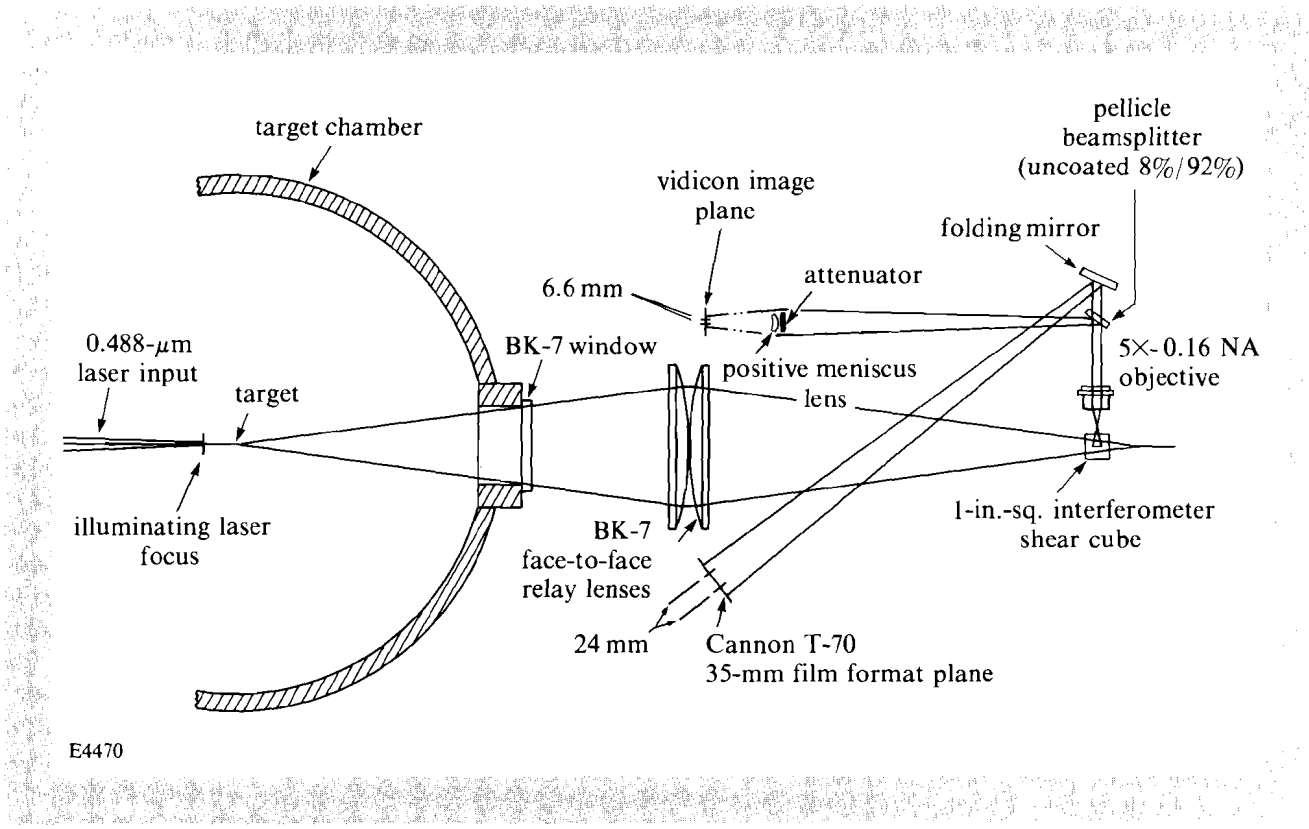

Fig. 33.13
Interferometer, as installed on the OMEGA target chamber.

design shown in Fig. 33.14 was invented. This could easily be made by photolithography and offered the advantage of a cheap, throwaway target mount. This type of target mount performed well thermally but exhibited small amplitude vibration during retraction. The shroud is normally pressurized to about 3 mTorr and is sealed at its open end by pressing against a stack of Mylar washers attached to the face of the target positioner cryostat extension (see Fig. 33.9). When the retraction begins, the gas starts to flow out through this annulus. In doing so, it causes very small amplitude flutter vibrations in the thin-copper target mount. These vibrations are soon coupled into the target-web system, setting up rather large (>100-μm) amplitude oscillations at frequencies >100 KHz. These problems were successfully diagnosed with a combination of high-speed multiframe photography, using a rotating drum camera, and single-frame photography, using a short-duration, high-power flash to illuminate the target as soon as it emerged from the shroud.

A potential solution to all of these problems is a new mount, which is currently under study. This is also an all-copper mount, soldered together using an indium/tin alloy solder but with a much thicker stem, to avoid the problems of aerodynamic movement. Tests on this mount will be conducted by the end of this quarter and cryo-target experiments, using this target mount, will begin shortly after the new year.

The most extensive redesign of the KMS-supplied equipment was in the retractor and retractor mount. As was mentioned earlier, problems

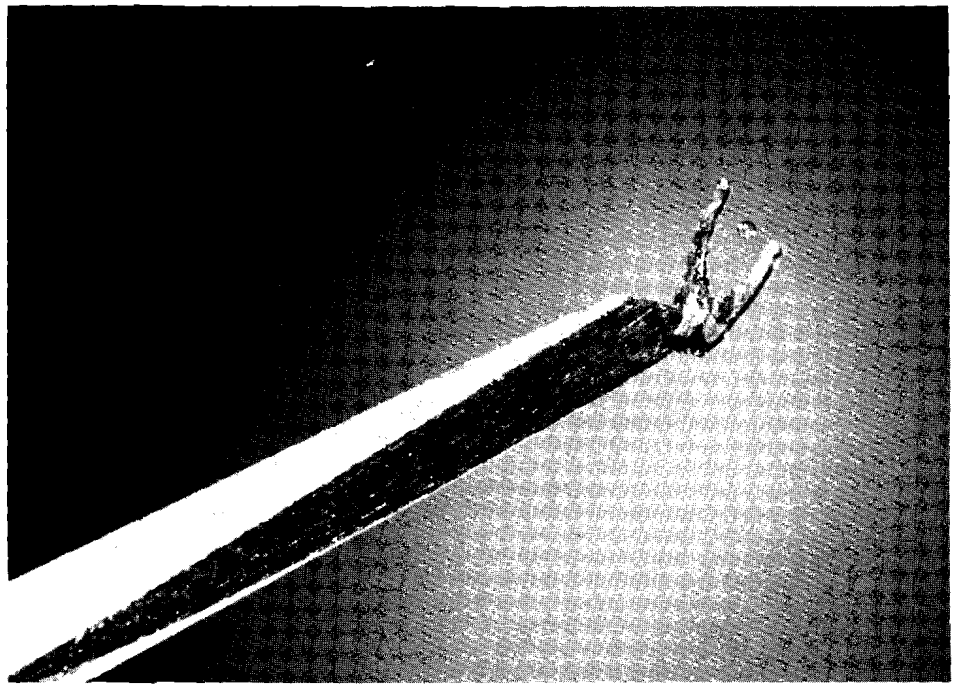

E4471

Fig. 33.14
Cryo target mounted on spider silks on thermally stable, photolithographically produced target mount.

arose early, with timing jitter and velocity uncertainty of the retractor. It was decided to replace the vacuum-powered retractor with a linear electric motor having a specification of 500 lb of pulling force and an acceleration of 10.6 g. Controlled deceleration was also specified, to minimize the impulse delivered to the mounting structure. The motor was to accelerate to maximum velocity for a distance of about 5 cm and then decelerate to zero velocity in an additional 5 cm. These specifications ensured that the shroud would be retracted to the fully clear position in less than 40 ms, resulting in a target exposure to 300°K radiation for about 4.8 ms. The motor also has an absolute positioning capability, which greatly speeds the insertion and positioning of the shroud over the target. The motor is completely computer controlled, with a standard serial interface providing the programming and hardware controls for commanding the retraction to begin. This motor was procured from Anorad[5] in slightly more than a month. New mounts were built to adapt the motor to the retractor and to the turning mirror structure. In slightly more than seven weeks after the decision to redesign, the new motor was installed and tested. It met or exceeded all specifications. LLE now has a retractor system capable of controlled, measured retractions that may lead to studies of targets in various phases of thawing. This system may be one way to achieve liquid-layer targets with a controlled amount of gas pressure in the void.

After only six months of operation, the cryo-target fabrication and positioning system has already begun to yield results in the LLE campaign to achieve high density with direct drive. Results from this campaign will be reported in a future LLE Review.

ACKNOWLEDGMENT

This work was supported by the U.S. Department of Energy Office of Inertial Fusion under agreement No. DE-FC08-85DP40200.

REFERENCES

1. KMS Fusion, Inc., P.O. Box 1567, Ann Arbor, MI 48106.

2. D. L. Musinski, T. M. Henderson, R. J. Simms, and T. R. Pattinson, in *Advances in Cryogenic Engineering*, edited by K. D. Timmerhaus and H. A. Snyder (Plenum Press, New York, 1980), Vol. 25, p. 49.

3. J. A. Tarvin *et al.*, in *Interferometry* (SPIE, San Diego, CA, 1979), Vol. 192, pp. 239–243.

4. D. L. Musinski *et al.*, KMS Fusion 1985 Annual Technical Report on Inertial Fusion Research, p. 97.

5. Anorad Corp., 110 Oser Avenue, Hauppauge, New York 11788.

Section 2
ADVANCED TECHNOLOGY DEVELOPMENTS

2.A The Design And Optimization of Recombination X-Ray Lasers

This article explores a number of theoretical issues crucial to the understanding and design of extreme-ultraviolet (XUV) recombination lasers. Our interest in this area was sparked by strong evidence that the Balmer-α line of hydrogen-like carbon at 182.3 Å was being amplified in plasmas produced in a series of exploding-foil experiments performed on OMEGA.[1] The targets consisted of a Formvar (polyvinyl formal, $C_{11}H_{18}O_5$) layer, which contains the carbon, and a selenium layer. The laser action was the result of recombination onto fully stripped ions of carbon.

The original goal of this experiment was to duplicate results obtained at the Lawrence Livermore National Laboratory, where amplification of fine-structure transitions of neon-like selenium was observed.[2] Consequently, the result indicating amplification of the carbon line was surprising, and it drew a prompt reaction from Nam *et al.*, who attributed the unexpected recombination behavior to rapid radiational cooling of the Formvar plasma by the selenium.[3] We have recently applied our hydrodynamic, atomic, and radiative-transfer modeling capabilities to this problem, to arrive at an understanding of this experiment and to explore recombination lasing as an option for future experiments at LLE. We will show the importance of radiative cooling relative to the importance of other effects, such as cylindrical expansion and lasant purity, in optimizing experiments to give the largest gain.

A carbon recombination laser is created by exploding a strip or fiber[4] of carbon with a line-focused laser beam to form a fully stripped carbon plasma. The plasma must be cooled to a temperature where it can recombine and expand to an electron density that favors collisional recombination to levels of the hydrogen-like species that are at or above the top of the inversion one wishes to create. Figure 33.15 illustrates a simplified level diagram of the hydrogen-like species as it is treated in the postprocessor described below. The arrows indicate the collisional and radiative processes connecting the various levels included in the atomic model. We seek to feed the levels above the $n=2$ level so that an inversion forms between the $n=3$ and $n=2$ levels of the Lyman-β transition. Lyman-α emission from the $n=2$ to $n=1$ transition depletes the lower level and deepens the inversion. On the other hand, the Lyman-α photons can be reabsorbed by photoexcitation of the same transition, which repopulates the $n=2$ level and destroys the inversion. Consequently, the plasma must be optically thin to this radiation. The cooling and expansion of the explosion must be rapid enough to bring the plasma to the desired range of conditions before most of the bare carbon has been recombined away.

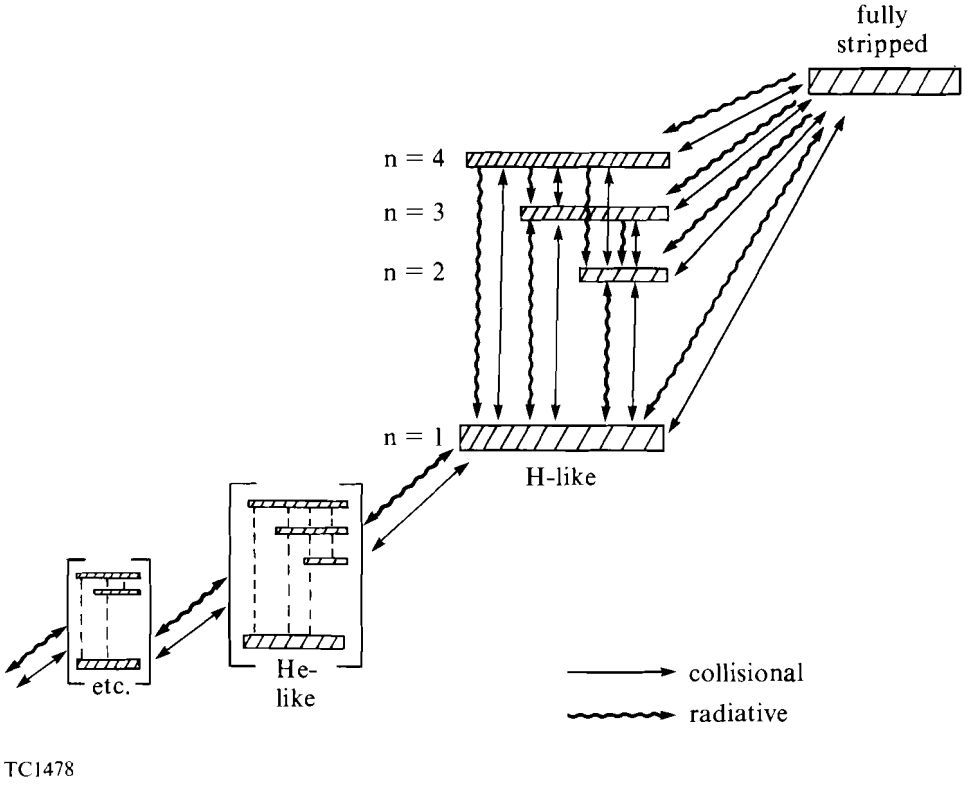

Fig. 33.15
Rate equations. The recombination pumping mechanism in hydrogen-like carbon, illustrated here, is simulated by the ionization and level-kinetics model in the non-LTE radiation postprocessor.

Whether or not it is possible to rapidly cool a hot plasma while bringing it to the right range of density without first having the lasant ions recombine away can be best answered by means of a full hydrodynamic simulation. The use of detailed modeling of laser-matter coupling and hydrodynamics in the one-dimensional hydrocode *LILAC*[5] establishes a credible connection between favorable lasing conditions in the target plasma and plausible experimental scenarios. The simulations are based on *LILAC* running with average-ion atomic physics and a radiative-transfer postprocessor that uses a detailed-configuration model of the ionic level populations and a line-of-sight solution to the equation of transfer to model the laser action. In Nam *et al.*,[3] which addresses the OMEGA experiment, the density and temperature histories are obtained from an idealized homogeneous one-zone model evolving from initial conditions that are not shown to be attainable with a real laser and target. Unlike all published simulations of similar experiments of which we are aware, we use a nonlocal model of the resonance-line photoexcitation of the lower level of the lasing transition. Emission- and absorption-line profiles are explicitly Doppler shifted according to the hydrodynamic velocity projected along the line of sight. The usual technique is to assume that the resonance emission either escapes or is reabsorbed within the zone where it originates, according to an escape probability that is calculated in terms of local plasma conditions and the local velocity divergence.[6] Other questions beyond the reach of one-zone semi-analytic calculations concern the spatial and temporal distribution of gain or—more specifically, whether the amplifying plasma is distributed broadly through the center of the plasma, whether only a small part of the plasma participates, whether amplification occurs in different parts of the plasma at different times, the lifetime of the gain, and so on. These questions arise in determining whether a pulse of light encounters amplifying plasma along the entire length of its travel through the plasma and in answering other questions regarding the net efficiency of a laser design.

Figure 33.16(a) shows schematically the configuration of the experiment of interest. A layered target consisting of a 0.075-μm selenium layer deposited on a 0.1-μm Formvar foil backing was illuminated from the selenium side along a strip 100-μm wide at an intensity of 7.0×10^{13} W/cm^2. Simulating this experiment in one dimension is not straightforward. A plane-parallel simulation, illustrated in Fig. 33.16(b), does not include the cylindrical divergence necessary for the expansion cooling of the plasma. To model the cylindrical divergence, simulations in cylindrical geometry, illustrated in Fig. 33.16(c), were performed. The target in this case is a cylinder made of the same layered foil as in the plane parallel case, rolled into a circumference equal to the irradiated width of the actual experiment. This results in the same amount of irradiated material per unit axial length of target and in the same irradiance on target at the original radius in the cylindrical simulation as in the actual experiment.

Two aspects of the cylindrical simulation that depart from the experiment are that the inner part of the cylinder implodes for a short time and that the target in the simulation must be homogenized

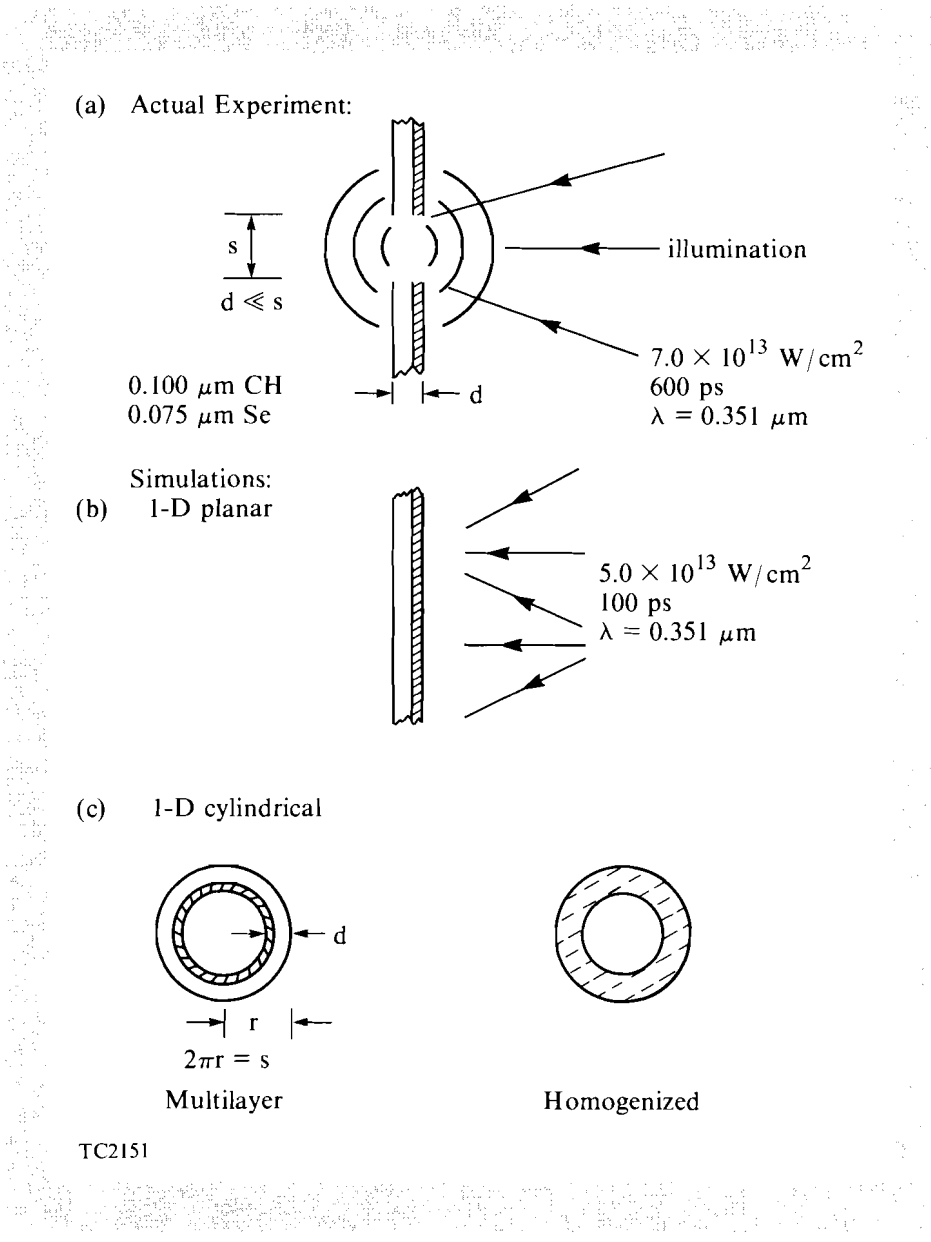

Fig. 33.16
Target geometries for 1-D simulation of cylindrical plasmas from exploding foils. Simulations in cylindrical geometry are used to model the cylindrical divergence of the foil exploding under line-focused illumination. Mixing is modeled by homogenizing the foil materials.

initially. The implosive episode in the simulation ends relatively quickly. By the time the plasma has expanded to the range of density of interest for recombination pumping at a diameter over 200 μm, details of the plasma conditions characteristic of this episode have smoothed away. Effects due to the initial geometry on the absorption of laser energy are at the level of fine tuning that is not of interest to the principles addressed in this article. Modeling the cylindrical expansion is a far more important consideration. Homogenizing the materials anticipates the mixing that is bound to occur to some degree and also serves as a compromise that allows materials from both layers to expand. Otherwise, the layer arbitrarily chosen to be the inner layer would be confined. It will be shown below that the carbon must mix with the selenium to some extent in order for the radiative cooling to be effective.

The hydrodynamic simulations employ a non-LTE average-ion model of the atomic physics. In this model, all ions of each element in a fluid zone are represented by a single ion whose level populations are the mean level populations of all such ions.[7] Our model includes the lowest ten principal quantum levels of each average ion. In glass, for example, the atomic description would consist of ten level populations for the average silicon ion and ten level populations for the average oxygen ion. In this manner, one can describe an arbitrary mixture of elements.

The level populations are calculated from time-dependent rate equations, including collisional ionization, recombination, excitation, and de-excitation; spontaneous emission; radiative recombination; and dielectronic recombination. The level energies are obtained using values of Slater screening coefficients[8] obtained by R. More.[9] Values of the rates are obtained from formulas appropriate for a screened hydrogenic approximation, where the active electron in a multi-electron ion is treated as if it were interacting only with a nucleus whose charge is determined from the nuclear charge and the effective screening of the spectator electrons, and where the multiplicities and vacancies of the participating levels are taken into account. Opacities and emissivities are calculated from the level populations. In the current version of the model, photoexcitation and photoionization are in the opacity model, but they are not coupled to the atomic rate equations. Following the example of Nam *et al.*, the emissivity due to fine-structure transitions is taken from a two-level model involving the ground state of the ion and the average of all levels representing a fine-structure excitation from the ground state.[3] Energies, statistical weights, and oscillator strengths for this average fine-structure transition are taken from Post *et al.*[10] The population of this average fine-structure excitation is obtained from the equilibrium between collisional excitation and decay and spontaneous emission. This contribution is expected to dominate the cooling in recombination-pumped lasing where the plasma cools to temperatures too low to excite transitions between the principal quantum levels at significant rates.

The output of the hydrodynamic simulation is fed into a postprocessor that calculates the atomic physics and radiative transport of the simulation in terms of a multispecies detailed-configuration atomic model capable of simulating the recombination pumping mechanism in the hydrogen-like species, and in terms of a line-of-sight integration of the equation of transfer capable of calculating the coupling of resonance radiation with the atomic-level populations.[11] This postprocessor has been upgraded to include the effects of the Doppler shift of emission and absorption line profiles on the photoexcitation rates. The hydrodynamic Doppler shift significantly increases the escape probability of carbon Lyman-α radiation, which would otherwise destroy the population inversion by populating its lower level.

A useful depiction of the behavior of an exploding carbon plasma is its trajectory in the temperature-density plane shown in Fig. 33.17(a).

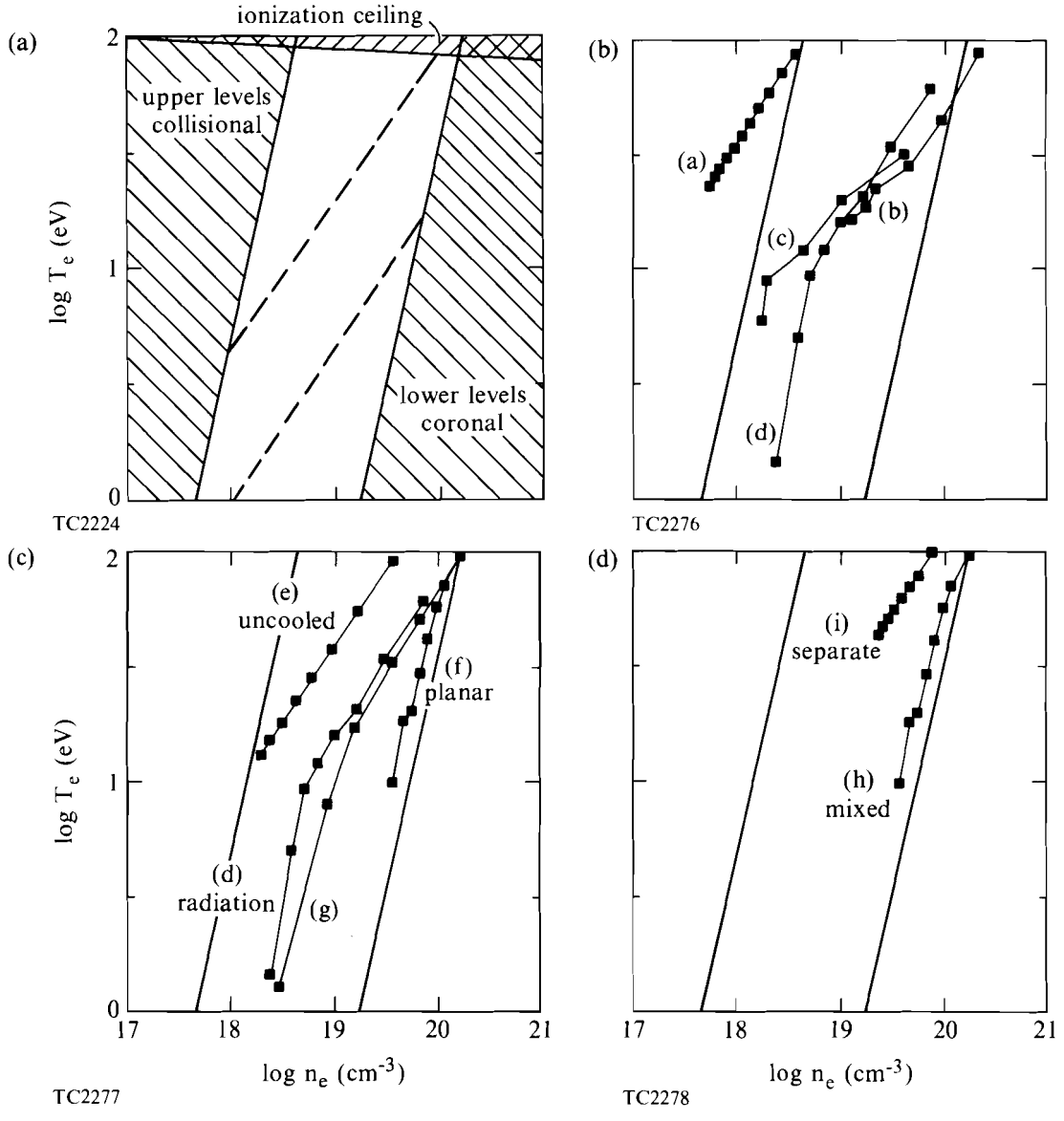

Fig. 33.17
Conditions permitting gain in the 3-to-2 transition at 182.3 Å in hydrogen-like carbon. Conditions allowing rapid recombination to the upper level of the inversion without close collisional coupling between the two inverted levels roughly define a region in the temperature-density plane where gain is expected. The overlays show trajectories of conditions obtained in various cases. Marks are placed every 200 ps. Cooling is delayed too long with a 600-ps pulse [curve (a)]. Conditions in the case of Nam *et al.* were obtained from an idealized one-zone simulation [curve (b)]. Conditions in the case of Lee and Estabrook were obtained from a hydrocode simulation of a case that gives good gain [curve (c)]. The case labeled "radiation" [curve (d)] is our example chosen to make comparisons illustrating the importance of various effects. Here, it is seen by comparison with an "uncooled" simulation [curve (e)] that radiative cooling is an important mechanism for cooling the plasma. Planar expansion does not lower the temperature quickly enough [curve (f)]. The best results were obtained from a simulation employing a pure carbon target [curve (g)]. Mixing of the lasant and coolant is required for radiative cooling to be effective [curves (h) and (i)].

From a few simple considerations, approximate limits on the useful area in the plane can be obtained. The labeled shaded areas indicate where inversion in the $n=3$ to $n=2$ interval cannot be achieved. Above the ionization ceiling, temperatures are too high for recombination to take place. To the left of the left-hand boundary, the collision rates are not high enough to have rapid recombination and rapid feeding of the upper lasing level from higher levels. To the right of the right-hand boundary, the collisional coupling of the $n=3$ to $n=2$ levels is rapid enough to destroy the inversion. The fact that collisional rates are more rapid for smaller transition and ionization energies allows an area where an inversion can be formed.

Plasmas enter this temperature-density diagram from the upper right as they expand and cool from a hotter, denser state. The optimum conditions are at temperatures below about 10 eV, where collisional excitation and collisional ionization contribute negligibly, and at electron densities slightly higher than 10^{19} cm^{-3}. As for all other relevant processes, the spontaneous emission rate is constant, and collisional recombination and de-excitation at low temperatures proceed according to rate coefficients that scale as $n_e/T_e^{1/2}$. Consequently, the level-population equations are invariant below about 10 eV along lines parallel to the left and right boundaries of the "allowed" area of the diagram. At lasing conditions that are near optimum, recombination of the bare carbon species is nearly complete well within one nanosecond, so not only must the plasma trajectory arrive near the 10 eV-10^{19} cm^{-3} point, it must arrive quickly, before the lasant supply has disappeared. The dashed lines in the diagram show the slope representing cooling of an ideal gas by adiabatic expansion. Since lines of constant collisional recombination rate fall along the steeper $n_e/T_e^{1/2}$ lines, the lasant supply must survive the passage through conditions where recombination occurs even faster than at the ideal destination. The gain coefficient is proportional to the degree of population inversion, as given by the difference in level population per unit statistical weight for the two levels in the lasing transition. The gain coefficient is also proportional to the spatial density of the lasant ions; for this reason, in addition to the above considerations, the highest gain occurs at the highest density that does not lead to collisional disruption of the inversion.

Curve (a) in Fig. 33.17(b) shows the trajectory of typical conditions in the exploding foil obtained in the simulation of the OMEGA experiment. The points on the curve are placed 200 ps apart. No gain is obtained in this plasma because it does not cool below the recombination ceiling until after it has expanded beyond the range of useful densities. This delay results from using too long a laser pulse because cooling cannot begin until after the pulse ends, even if the plasma has expanded below the critical density for the illumination wavelength.[12]

The observation of gain in an exploding-foil target under irradiation as long as 600 ps is a mystery at this time. There is no indication that pulses this long could ever allow the exploded foil to cool quickly enough. On the other hand, shorter pulses of 100 ps, for example, can

produce amplifying plasmas, which tempts speculation that some unanticipated diversion of the laser illumination away from the plasma could have allowed the plasma to cool. We will not delve further into exotic explanations that we can neither substantiate nor rule out. Instead, we leave this problem as an interesting puzzle for future work and confine our attention to illumination pulses of 100 ps and to simulations that do produce gain.

An optimized case obtained by Nam *et al.*[3] is represented by the trajectory [curve (b)] [Fig. 33.17(b)], again with points placed 200 ps apart. These conditions do produce gain, in contrast to the conditions in curve (a) [Fig. 33.17(b)], but because they represent a one-zone model of a plasma expanding from an ad hoc initial configuration, there remains the question of whether they can be duplicated in a more realistic simulation of a plasma exploded from a foil by a laser. Qualitatively, this trajectory is a typical favorable case. The density drops quickly into the favorable area so that the loss of bare carbon is minimal. Even though radiative cooling is comparable to expansion cooling in this plasma, the trajectory remains roughly parallel to the adiabatic slope. Presumably, radiative losses are countered by the electron binding energy released by collisional recombination and decay. Another favorable trajectory [curve (c)], shown in Fig. 33.17(b), represents a single Lagrangian zone in the plasma ablated off the surface of a carbon fiber simulated by Lee and Estabrook using a hydrocode.[13] It is interesting that the two trajectories show a similarity not only to each other, but to that of our chosen example, shown in Fig. 33.17(b) [curve (d)].

Figure 33.17(c) shows by comparison the effect of radiative cooling on one case simulated on *LILAC*. The case labeled "radiation" is the standard case given by curve (d) in Fig. 33.17(b). This simulation employs a foil 0.175-μm thick, composed of the same thicknesses of CH and selenium as in the original OMEGA experiment, homogenized and rolled into a cylinder 15.9 μm in radius. The UV (0.351-μm) illumination has been reduced to 5.0×10^{13} W/cm^2 at a pulse length of 100 ps. The plotted conditions are taken from the history of one of the Lagrangian zones near the center of the foil where gain was obtained. Comparison of the "radiation" and "uncooled" trajectories shows that the desired higher density results from the additional cooling. The trajectory labeled "uncooled" [curve (e)] represents the same length of time as the standard case, but it follows an ideal-gas adiabat, while the standard case eventually falls more rapidly and more steeply as radiative cooling overtakes the adiabatic cooling. In this case, at least, it is clear that radiative cooling can be a useful device for shaping the trajectory. While under conditions that permit gain due to recombination pumping, any lowering of the temperature reduces collisional excitation and ionization rates relative to the pumping rates and also reduces the pressure that drives the plasma to lower densities where the pumping rates and the lasant ion density are lower.

Curve (f) in Fig. 33.17(c) shows the plane-parallel counterpart of the standard case illustrated in curve (d). The comparison shows that cylindrical expansion is the dominant cooling mechanism, even in the

presence of radiative cooling, and that planar expansion is not nearly as effective. The "planar" trajectory moves into a region of good conditions for gain, but cooling is too slow to keep the lasant from being depleted by recombination.

Figure 33.17(d) shows a comparison of trajectories for two plane-parallel simulations. The "mixed" case [curve (h)] is the same as the standard case, except that the foil is unrolled and the one-dimensional simulation geometry is planar. The companion "separate" case [curve (i)] is identical, except that the selenium and plastic are separated as in the original experiment. Both trajectories are relatively slow because planar expansion is not as fast as cylindrical expansion. In the mixed case, radiative cooling pulls the trajectory down from the adiabat. In the separate case, the trajectory for a central zone in the CH layer is very nearly adiabatic. Even though there is radiative cooling in the selenium, the thermal contact with the carbon-containing layer is not effective. This shows that mixing is essential if radiative cooling is to work under the conditions of interest.

Curve (g) in Fig. 33.17(c) shows the trajectory for a case that yields the highest gain obtained in our calculations. Details of this simulation are given below. The expansion is very rapid, and the cooling is slightly faster than adiabatic. The cylinder is made of pure carbon and has half the radius of the standard case so that the rate of relative expansion is more rapid.

In the standard case, gain occurs in a cylindrical region starting about 300 μm from the center of the plasma about 840 ps after the peak of the pulse, or at 1.0 ns into the simulation as shown in Fig. 33.18(a). The points represent individual Lagrangian zones. The gain profiles rise at this radius and then spread outward. Figure 33.18(b) shows the results of a calculation identical in every respect, except that the pumping of the lower level due to absorption of the Lyman-α emission of hydrogen-like carbon is neglected. Comparison of the two figures provides a good illustration of the damaging effects of photoexcitation. The results, including photoexcitation, are almost identical with the results ignoring this effect, except that additional expansion is needed to raise the Lyman-α escape probability. This can be observed more easily in Fig. 33.19, where the gain profiles are seen to become very nearly the same after 1.4 ns. This behavior is similar to that obtained using local escape probability approximations.[3] It is significant that a nonlocal treatment gives similar results. Even though the local and nonlocal models are quite different, the differences would affect the results under conditions intermediate between those giving certain capture and certain escape. In this case, the plasma passes through the intermediate state quickly enough for the differences to escape notice.

Figure 33.20 shows that significant improvement can be obtained by reducing the amount of cylinder material, the carbon in particular, so that the plasma need not expand as far to become optically thin to the carbon Lyman-α. By removing the hydrogen, leaving a carbon/selenium mixture, the spatial density of carbon at the lasing density is increased slightly, which also increases the gain.

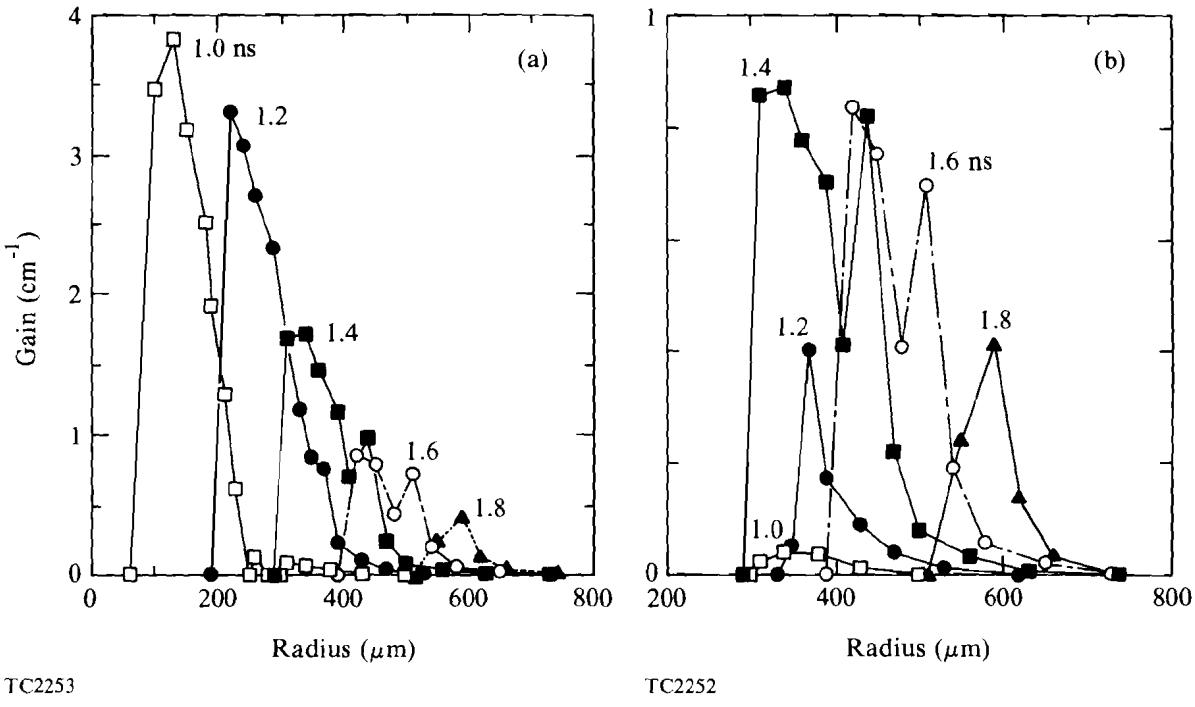

Fig. 33.18
(a) Profiles of gain at 182.3 Å in an exploding CH/Se cylinder; free escape. Gain occurs in a fairly narrow region that moves through the plasma.
(b) Profiles of gain at 182.3 Å in an exploding CH/Se cylinder; Doppler-assisted escape. Radiative capture of carbon Lyman-α reduces the gain at earlier times.

Carrying the optimization one step further, we obtain the very much improved gain profiles shown in Fig. 33.21. The trajectory for this simulation is shown as curve (g) in Fig. 33.17(c).

The target has been reduced to a thickness of 0.045 μm and a radius of 8.0 μm. The target is pure carbon, with no coolant. A greatly reduced driver intensity of 0.05 TW/cm is permitted. What is particularly interesting about this simulation is that the gain peaks simultaneously throughout the entire plasma, rather than in a wave, as in the previous cases. The net amplification by a laser is dependent on the shape of the gain profile, and the possible advantages of having gain peak simultaneously throughout the plasma would be an interesting question to pursue. This particular target is probably too frail to construct, but it illustrates how far the optimization can be taken. A more realistic target from the fabrication standpoint is a solid fiber of roughly this diameter.[4,13] Ideally, one would form a plasma such as this by ablating a thin layer off the fiber, leaving most of the original target behind.[14]

The high gain of this last case, illustrated in Fig. 33.21, can be attributed in part to the fact that the foil is pure carbon. Removing the selenium entirely defeats the radiative cooling, but increases the carbon density roughly threefold under the lasing conditions because the selenium had been contributing almost four times as many free electrons per ion as the carbon.

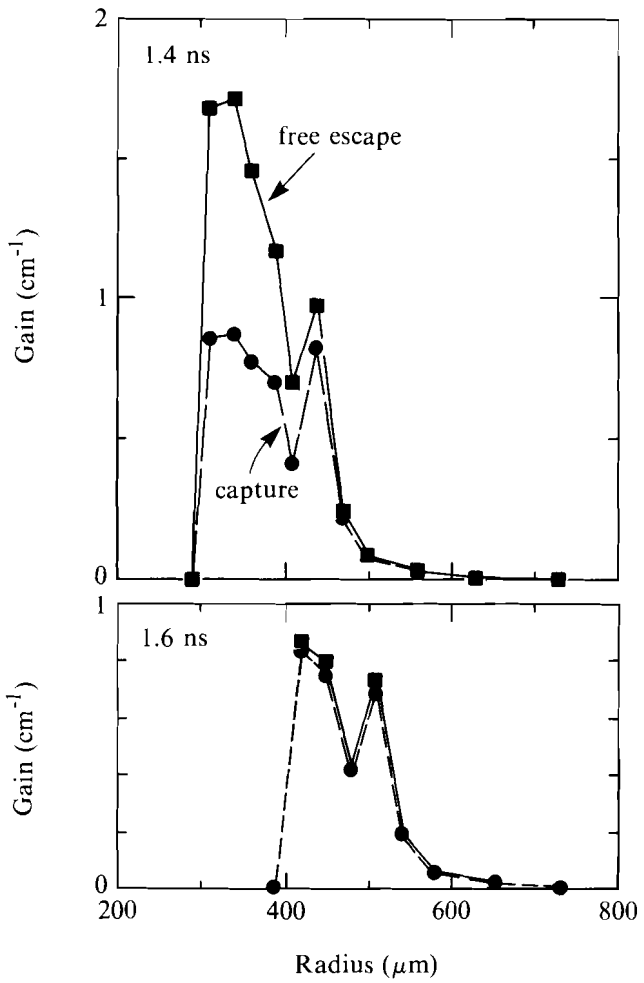

TC2254

Fig. 33.19
Profiles of gain at 182.3 Å in an exploding CH/Se cylinder. The effect of radiative capture on gain is negligible at later times.

While much has been shown about what affects the performance of carbon XUV lasers, the observed evidence for gain using 600-ps pulses from OMEGA on foil targets remains a puzzle. Perhaps there is a means by which the illumination becomes ineffective after a much shorter time. Lasing driven by 100-ps illumination has been modeled, and it is clear that cylindrical expansion is the most important cooling mechanism. Cooling by a radiating impurity does work if it is mixed with the carbon, but diluting the lasant can reduce the gain coefficient significantly. No new behavior was obtained by using an explicit, nonlocal treatment of photoexcitation. For exploding plasmas of the kind considered here, models of photon-escape probability based on local conditions and on the local value of the velocity divergence are adequate. The transition from strong photon confinement to certain escape is rapid in both local and nonlocal treatments, so the distinctions are not important. Nevertheless, as the optical depth of the expanding plasma drops, there is a period of time where photon paths

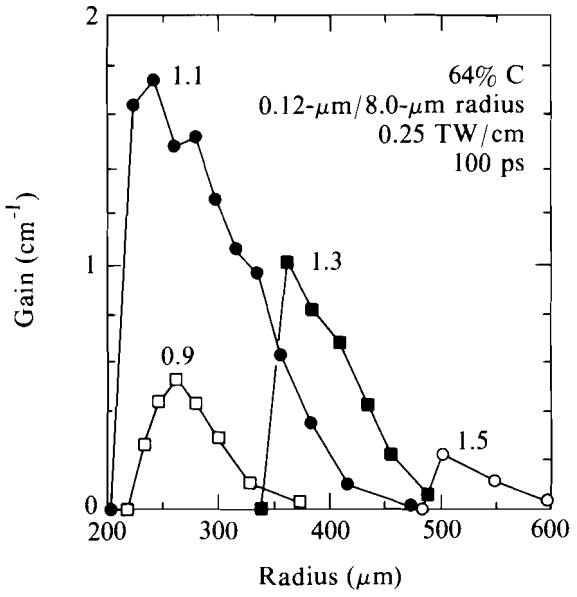

TC2268

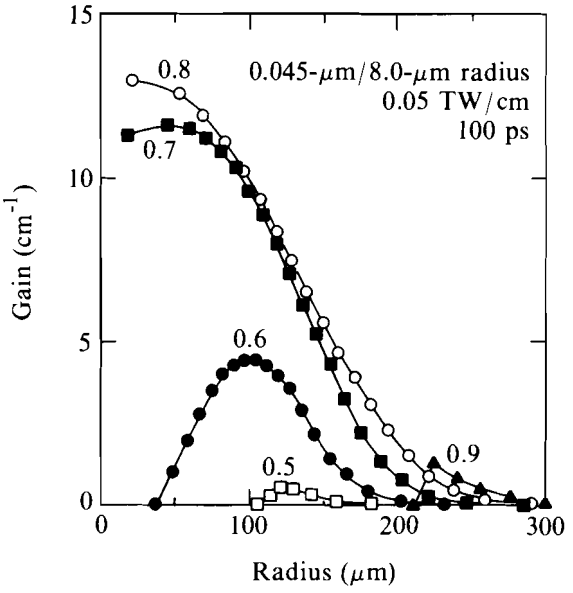

TC2272

Fig. 33.20 (left)
Profiles of gain at 182.3 Å in an exploding C/Se cylinder. Gain is increased by removing the hydrogen, which dilutes the lasant and does not contribute to radiative cooling, and by decreasing the mass per length of the plasma, which increases the escape probability of the carbon Lyman-α radiation.

Fig. 33.21 (right)
Profiles of gain at 182.3 Å in an exploding carbon cylinder. Gain is greatly increased by removing the selenium entirely. This defeats the radiative cooling, but increases the carbon density roughly threefold under the lasing conditions because the selenium had been contributing almost four times as many free electrons per ion as the carbon.

are no longer short, compared to the plasma size, but where escape is still unlikely. Under such conditions, a local approximation does not apply, and it becomes appropriate to adopt a nonlocal model such as has been done here.

ACKNOWLEDGMENT

This work was supported by the Naval Research Laboratory under contract No. N0014-86-C-2281.

REFERENCES

1. J. F. Seely, C. M. Brown, U. Feldman, M. C. Richardson, B. Yaakobi, and W. E. Behring, *Opt. Commun.* **54**, 289 (1985).
2. D. L. Matthews *et al.*, *Phys. Rev. Lett.* **54**, 110 (1985); M. D. Rosen *et al.*, *ibid.* **54**, 106 (1985).
3. C. H. Nam, E. Valeo, S. Suckewer, and U. Feldman, *J. Opt. Soc. Am. B* **3**, 1199 (1986).
4. G. J. Pert, *J. Phys. B* **9**, 3301 (1976).
5. An earlier version of *LILAC* is described in Laboratory for Laser Energetics Report No. 16, 1976.
6. V. V. Sobolev, *Astron. Zh. Sov. Astron.* **24**, 13 (1947), cited in V. A. Ambartsumian, *Theoretical Astrophysics* (Pergamon, New York, 1958), p. 490.
7. W. A. Lokke and W. A. Grasberger, Lawrence Livermore National Laboratory Report No. UCRL-52276, 1977 (unpublished).

8. J. C. Slater, *Phys. Rev.* **36**, 57 (1930).

9. R. M. More, *J. Quant. Spectrosc. Radiat. Transfer* **27**, 345 (1982).

10. D. E. Post *et al.*, *At. Data Nucl. Data Tables* **20**, 397 (1977); C. H. Skinner and C. Keane, *Appl. Phys. Lett.* **48**, 1334 (1986).

11. R. Epstein, S. Skupsky, and J. Delettrez, *J. Quant. Spectrosc. Radiat. Transfer* **35**, 131 (1986).

12. R. A. London and M. D. Rosen, *Phys. Fluids* **29**, 3813 (1986).

13. R. W. Lee and K. G. Estabrook, *Phys. Rev. A* **35**, 1269 (1987).

14. G. J. Pert, *J. Opt. Soc. Am. B* **4**, 602 (1987).

2.B Near-Infrared Dichroism of a Mesogenic Transition Metal Complex and Its Solubility in Nematic Hosts

Introduction

The use of dichroic dyes in guest-host liquid-crystal displays has received a great deal of attention in recent years. Numerous literature references[1-7] can be found regarding the order parameter, dichroism, solubility, and stability of a wide variety of dyes in nematic and smectic hosts for electro-optical applications in the visible region of the spectrum. Little information is available, however, regarding applications in the near-infrared region of the spectrum,[8] such as the blocking or modulation of diode or YAG laser sources. One reason for this lack of information is the limited availability of dyes with strong electronic absorption bands in this region. One class of materials that displays strong near-infrared absorption bands with molar extinction coefficients (ϵ) for these bands of nearly 30,000 is the square-planar transition metal dithiene complexes[9] generically shown in Fig. 33.22.

The position of the absorption band in these materials can vary from 750 to 1075 nm, depending on the molecular structure of the ligands and, to a much lesser extent, on the particular central metal atom in the complex.[9] A well-known example of this class of compounds is the laser dye bis(dimethylaminodithiobenzil)nickel [Fig. 33.23(a)], which possesses an absorption maximum at 1064 nm. Several of the dithiene transition-metal complexes display mesomorphic behavior; Ohta *et al.*[10] have reported discotic mesomorphism in the bis[1,2-di(*p*-*n*-alkoxyphenyl)ethane-1,2-dithione]nickel complexes [Fig. 33.23 (b)], and Giroud-Godquin *et al.* have reported the occurrence of nematic[11-13] and smectic[11-16] phases in the bis(*p*-*n*-alkylstyryl-1,2-dithiolato)nickel and platinum complexes [Fig. 33.23(c)].

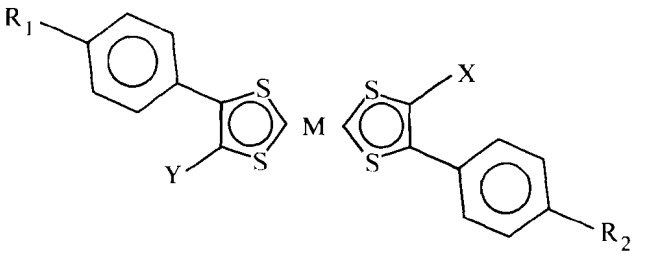

M = Ni, Pt, Pd, Cu
X and Y = H or substituted phenyl
R_1 and R_2 = alkyl, alkoxyl, alkylamino, cyano, etc.

G2113

Fig. 33.22
General molecular structure of the transition metal dithienes.

(a)

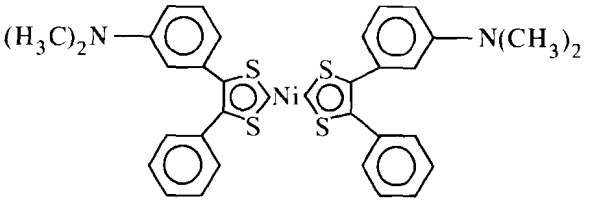

(b)

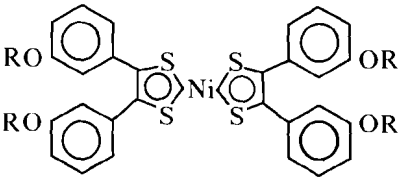

(c)

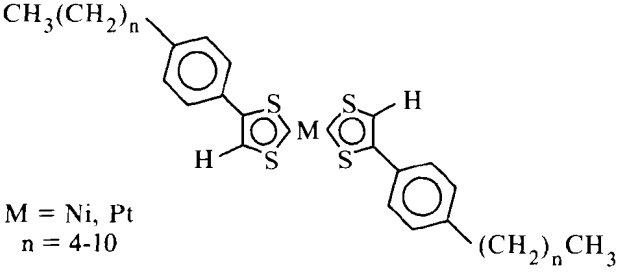

M = Ni, Pt
n = 4-10

G2114

Fig. 33.23
Molecular structures of various dithiene complexes. (a) bis(dimethylaminodithiobenzil)nickel; (b) bis[1,2-di(*p*-*n*-alkoxyphenyl)ethane-1,2-dithione]nickel; (c) bis(*p*-*n*-alkylstyryl-1,2-dithiolato)nickel and platinum.

Although several references[11,15,17] suggest the potential usefulness of these metal complexes in mixtures with themselves or with other liquid-crystal materials for near-infrared switching applications, there has been to date no report of the dichroic behavior of these metal complexes in nematic host materials. Complexes of structure (c) (see Fig. 33.23) would be of particular interest for this application for several reasons:

1. The elongated rodlike structure of these metal complexes, combined with the extensive electron delocalization afforded by the metal dithiene core, would be expected to promote the occurrence of positive dichroism in the strong near-infrared absorption band of these materials.

2. The high solubility of these complexes in nonpolar solvents such as hexane[11,14,15] indicates they may be highly soluble in the relatively nonpolar liquid-crystal hosts, which themselves display a high solubility in hydrocarbon-like solvents. Typical guest-host and laser dyes are soluble to a great extent only in such polar solvents as methanol or chloroform, and display little if any solubility in nonpolar solvents. As a result, the maximum stable dye concentration obtainable with most dichroic dyes in liquid-crystal hosts is typically around 1% to 2% by weight.[1,2]

3. The presence of a stable nematic phase with a wide mesomorphic range (117°C–178.6°C in the *n*-butyl derivative)[16] would allow the addition of large quantities of the metal complex to increase mixture absorbance without causing the major reduction in the mixture transition temperature and order parameter that would occur with a large addition of a non-mesogenic dye of equivalent solubility.

We have undertaken the synthesis of one of the members of this interesting series, bis(*p*-*n*-butylstyryl-1,2-dithiolato)nickel (abbreviated as C_4-Ni), and studied its behavior in the well-known nematic liquid crystals K15 (BDH Chemicals) and MBBA (Aldrich Chemical Co.). The solubility, optical absorption characteristics in the 800-nm to 1100-nm region, and stability of the mesogenic metal complex in these nematic hosts were determined and compared to similar data obtained for the laser dye bis(dimethylaminodithiobenzil)nickel (DMADB-Ni, Eastman Kodak Co.) in K15. We have also observed what we belive to be the first reported evidence of positive near-infrared dichroism in mesomorphic metal dithiene complexes in a nematic host.

Experimental

Liquid-crystal phase characterization and transition temperature measurements were determined using a Leitz Orthoplan Pol polarizing microscope and a Mettler FP-52 hot stage. Infrared spectra were obtained with a Nicolet 20SXC FTIR spectrometer. A Perkin-Elmer Lambda 9 UV-VIS-NIR spectrophotometer was used for absorption measurements of the metal complex and mixtures, and for the measurement of the dichroic ratio.

1. Synthesis

The liquid-crystal metal complex C_4-Ni was synthesized by a method described by Giroud-Godquin and Mueller-Westerhoff.[11,15] The synthesis scheme is outlined in Fig. 33.24. The ratio of dioxane to water in the reaction mixture during complex formation had a considerable effect on the formation of product; initial yields of 1%–2% obtained with only small amounts of water in the reaction mixture were improved to 10% by using a dioxane/water ratio of 1:1. The use of a nitrogen purge during the reaction of *p-n*-butylphenacyl bromide with phosphorous pentasulfide, and the subsequent reaction with nickel chloride, helped to minimize the formation of tarry side products. Isolation of the product was accomplished by extracting the reaction mixture several times with a 1:1 toluene-hexane mixture. After evaporation of the extracts under vacuum, hexane was added to the residue and the soluble portion was chromatographed on silica gel, with hexane as the eluent. The dark green fraction was collected and the solvent evaporated. A dark green residue was obtained, which was recrystallized several times from hexane to yield shiny, nearly black needles. The product exhibited a C-N (crystalline-nematic) transition at 117°C; an irreversible nematic-isotropic transition occurred at 178.7°C due to thermal decomposition of the complex. These results are consistent with those reported earlier for this material.[11,14–17] The purity of the product was qualitatively assessed by thin-layer chromatography on plates of silica gel with hexane as the eluent. Only one spot was observed after development of the plates with iodine vapor. The infrared spectrum of the complex in KBr showed extremely strong bands at 1365 and 1198 cm^{-1}, which were assigned to perturbed $C = C$ and $C = S$ stretching caused by bond formation between the central metal atom and the sulfur ligands.[9] The visible-NIR spectrum of a 1-cm path length of a 50-ppm solution of the complex in hexane displayed the strong near-infrared absorption band (optical density = 2.81) characteristic of this class of compounds, which for this material occurs at 860 nm.[9,11,14–17] The molar extinction coefficient ϵ of ~28,000 was calculated for the complex based on the above absorbance data using the Beer-Lambert law, $A = \epsilon bc$, where A is the absorbance in optical density units, b is the path length in centimeters, and c is the concentration expressed in moles per liter.

2. Mixture Preparation

Mixtures of various concentrations (0%–10% wt/wt) of C_4-Ni in the nematic hosts K15 and MBBA were prepared by dissolving the complex in the host material at 50°C and stirring the resulting mixture for one hour. The host materials were used as supplied without further purification. The mixtures were cooled and were allowed to stand at 20°C for several days to avoid supersaturation. All samples were filtered through Teflon membrane filters (0.5-μm pore size) prior to making absorption spectroscopy measurements, in order to remove insoluble foreign material and precipitated dye crystals. Absorption measurements were repeated on samples stored in glass vials for one month after filtration through 0.5-μm-pore Teflon membrane filters. The above procedure was also used for the preparation of mixtures of the near-IR laser dye DMADB-Ni in K15.

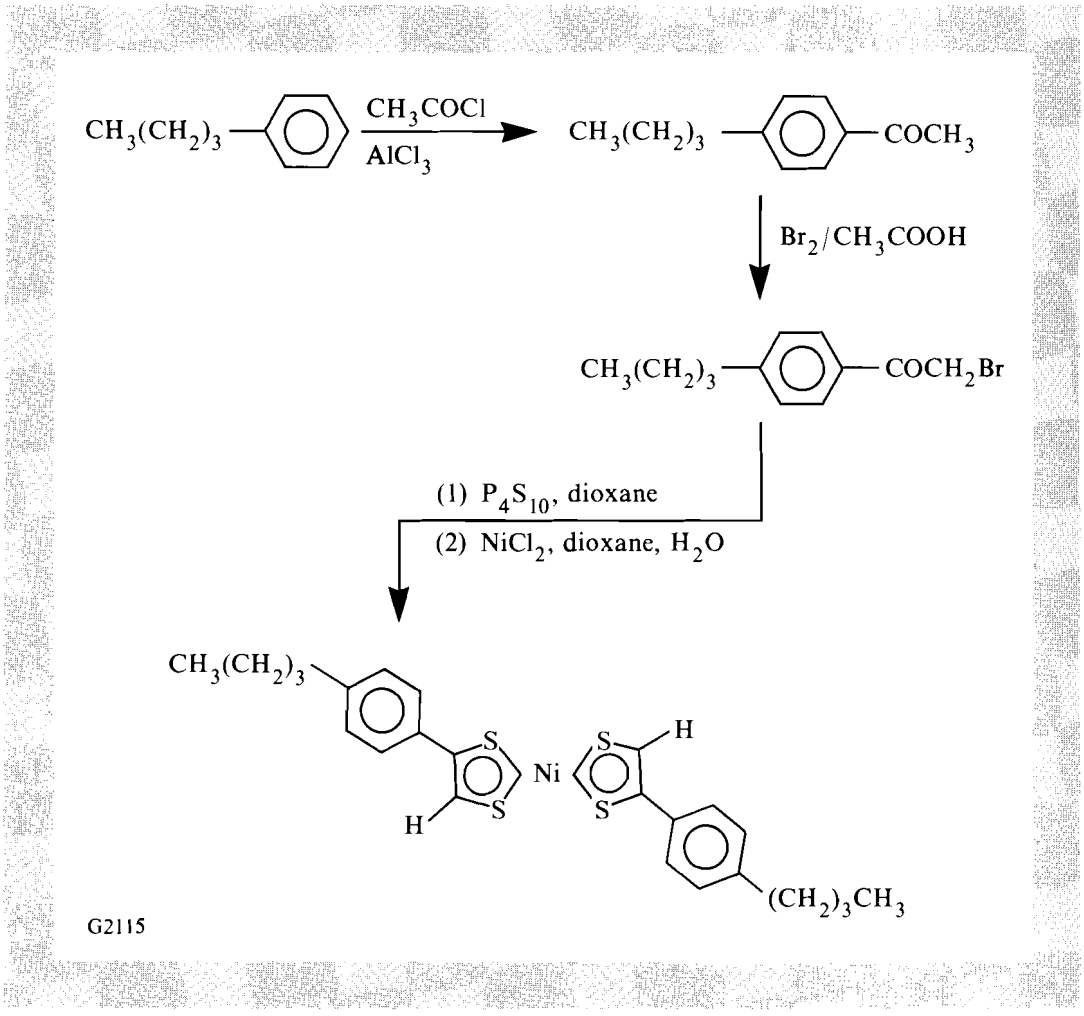

Fig. 33.24
Synthesis method for the preparation of bis(*p*-*n*-butylstyryl-1,2-dithiolato)nickel.

3. Absorption Spectroscopy

The visible and near-IR absorption characteristics of the mixtures in the isotropic state were determined in 100-μm-path-length quartz spectrophotometer cells at 50°C in a heated sample compartment in the spectrophotometer. This method, rather than the addition of solvent diluents, was used to eliminate optical scatter produced by the unaligned bulk liquid-crystal material, since complications such as dilution errors, solvent effects on absorbance maxima positions, and introduction of impurities into the mixtures are avoided. The near-infrared spectra displayed inherent lead sulfide detector noise at optical density (OD) values of 3 or greater. The raw spectral data was used without additional smoothing.

4. Dichroism Measurement

The dichroism of the NIR absorption band was determined in a homogeneously aligned cell containing a 1% wt/wt mixture of C_4-Ni in K15. The homogeneous alignment condition was obtained using a rubbed PVA alignment layer, which was applied to indium tin oxide (ITO) conductive-coated substrates (2 cm × 2 cm) by spin deposition. The cell was assembled with the rub directions antiparallel and filled by capillary action, with the fluid gap of 24 μm controlled by Mylar

spacers. Measurements of absorption in the homogeneous and homeotropic orientations were made in the spectrophotometer sample chamber, with the cell rub axis parallel to a Corning Glass 8612 IR polarizer aligned parallel to the inherent spectrophotometer beam polarization. Switching into the homeotropic orientation was accomplished by the application of a 10-V, 100-KHz-square wave provided by a Tektronix FG-508 function generator. Absorption spectra, corrected for Fresnel and ITO coating absorption losses, were obtained after subtraction of a stored background spectrum of two index-matched ITO-coated plates from the raw absorbance data.

Results and Discussion

1. Physical Properties of the Mixtures

A series of mixtures containing C_4-Ni in K15 and MBBA ranging in concentration from 0.5% to 10% wt/wt was prepared as described in the experimental section. Mixtures of the laser dye DMADB-Ni in K15 and MBBA were prepared by the same method for use as a benchmark for the comparison of solubility and absorption properties. Mixtures containing amounts as large as 5% and 10% wt/wt of C_4-Ni in K15 showed no apparent signs of separation of the dye complex, even after storage at 20°C for one month. No precipitation or separation of the dye component was observed either in the containers or upon observation of agitated samples of the mixtures by polarizing microscopy at 100X magnification. In contrast, a mixture of DMADB-Ni in K15 began to show signs of separation immediately after cooling to room temperature, and a nearly complete precipitation of the dye was observed after the mixture had been allowed to stand for several days. The stable concentration limit of DMADB-Ni in K15 was determined to be 0.05% wt/wt, by making absorption spectroscopy measurements of filtered samples and comparing the results against known standards. We attribute this large disparity in solubility between C_4-Ni and DMADB-Ni in the nematic hosts to be due in part to differences in the molecular structures of the two complexes. Referring to Fig. 33.23, the rodlike nature and alkyl terminal groups of C_4-Ni [structure (c)] would be expected to promote solubility in the hydrocarbonlike nematic materials. The terminal dimethylamino groups of DMADB-Ni [structure (a)] introduce a high degree of polarity due to the unshared electron pair on the nitrogen atom, and, thus, should favor solubility in polar solvent matrices (e.g., chloroform or methanol). The presence of the two additional phenyl groups give DMADB-Ni a disklike structure, which would not fit as well as C_4-Ni into the nematic liquid-crystal matrix.

The effect of the concentration of C_4-Ni in K15 and in MBBA on the mixture transition temperatures can be observed in Fig. 33.25. The presence of the nematic metal complex causes a gradual increase in mixture transition temperature with increasing concentration, as would be expected due to the large mesomorphic range and high N-I transition temperature (117°C–178°C) of C_4-Ni. The slope of the transition temperature versus concentration curve for the K15 mixtures is considerably larger than for MBBA mixtures at the same concentration, causing us to speculate that an interaction was taking place between MBBA and C_4-Ni. This speculation was confirmed

when, after examination of samples, which had been stored in glass vials under ambient conditions for one month, it was discovered that the MBBA mixtures had changed color from dark green to reddish brown, with a black, tarry precipitate evident in the 5% and 10% wt/wt samples. The K15 mixtures stored under the same conditions appeared unchanged. In Figs. 33.26(a) and 33.26(b), the transition temperatures of the new and one-month-old mixtures of C_4-Ni in K15

Fig. 33.25
Dependence of mixture N-I transition temperature on metal complex concentration for various compositions of C_4-Ni in K15 and MBBA.

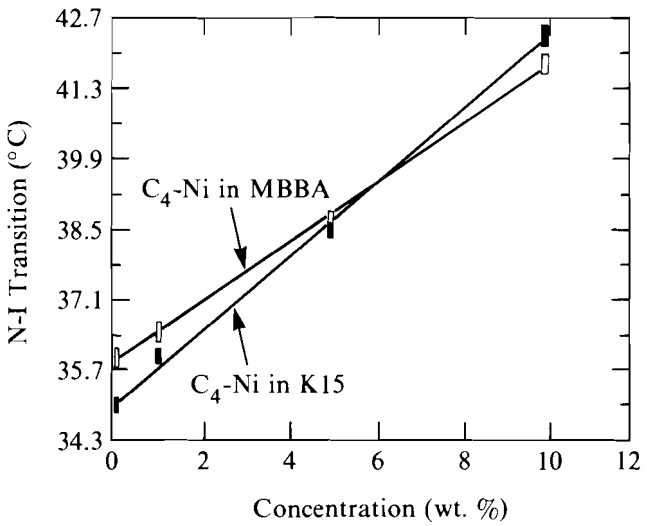

Fig. 33.26
Effect of aging on the N-I transition temperature of C_4-Ni/K15 and C_4-Ni/MBBA mixtures as a function of metal complex concentration. (a) New and one-month-old mixtures in K15; (b) new and one-month-old mixtures in MBBA.

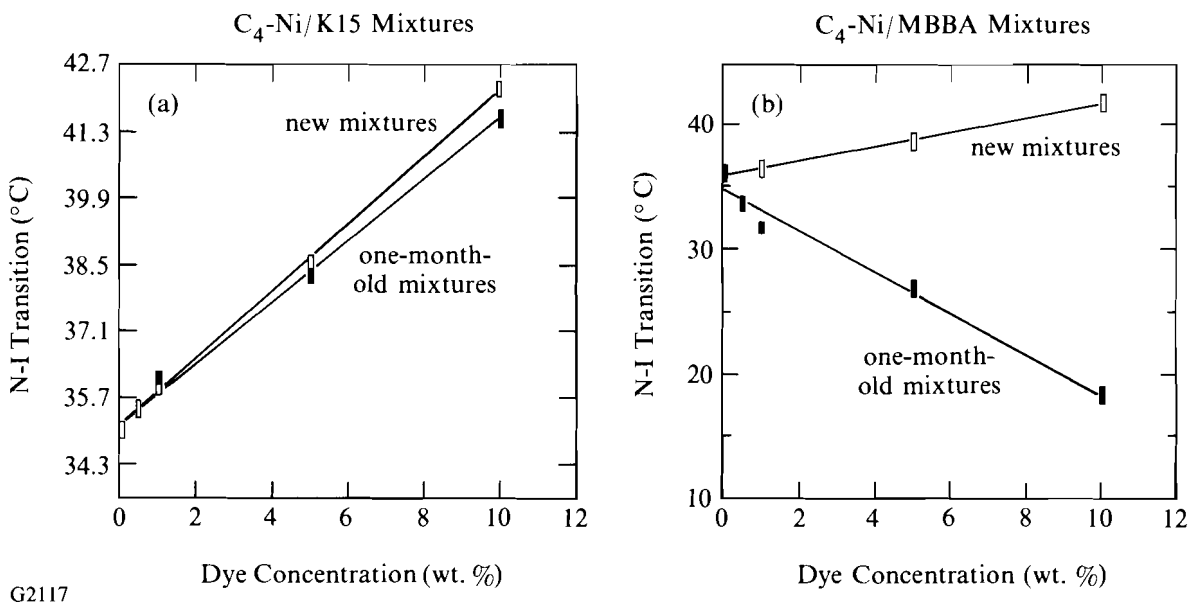

and MBBA mixtures are plotted as a function of metal complex concentration. The K15 mixtures show a slight decrease in transition temperature with time (a maximum of 0.8°C for the 10% wt/wt mixture), while large reductions in the N-I transition are evident for even the most dilute C_4-Ni/MBBA mixtures. The transition temperature of the most concentrated C_4-Ni/MBBA mixture (10% wt/wt) was depressed by over 23°C from its original value, rendering it isotropic at room temperature. The change observed in the visible and near-IR spectra of the one-month-old MBBA mixtures (discussed in detail in the following sections) and the radical reduction in transition temperature for the C_4-Ni/MBBA mixtures indicate a chemical reaction has apparently occurred between these compounds, resulting in the formation of isotropic reaction products. The nature of this reaction is the subject of current investigations. The dianions of these complexes have been reported by Schrauzer[9] and others[18] to readily undergo nucleophilic substitution reactions with other materials; this suggests that reduction of the metal complex may be an important step in the degradation process.

2. Absorbance Spectroscopy

The effect of the solvent matrix on the position of the absorption maximum for C_4-Ni is illustrated in Fig. 33.27. A bathochromic shift is observed for freshly prepared samples of C_4-Ni in K15 and MBBA scanned in the isotropic phase (50°C), as compared to a 50-ppm solution of the complex in hexane. The reduced absorption band for the C_4-Ni/MBBA mixture, as compared to an equivalent C_4-Ni/K15 mixture at the same concentration (0.5%), indicates that the reaction between the metal complex and MBBA may begin upon initial mixing. The absorption curves of new and aged samples of C_4-Ni in the

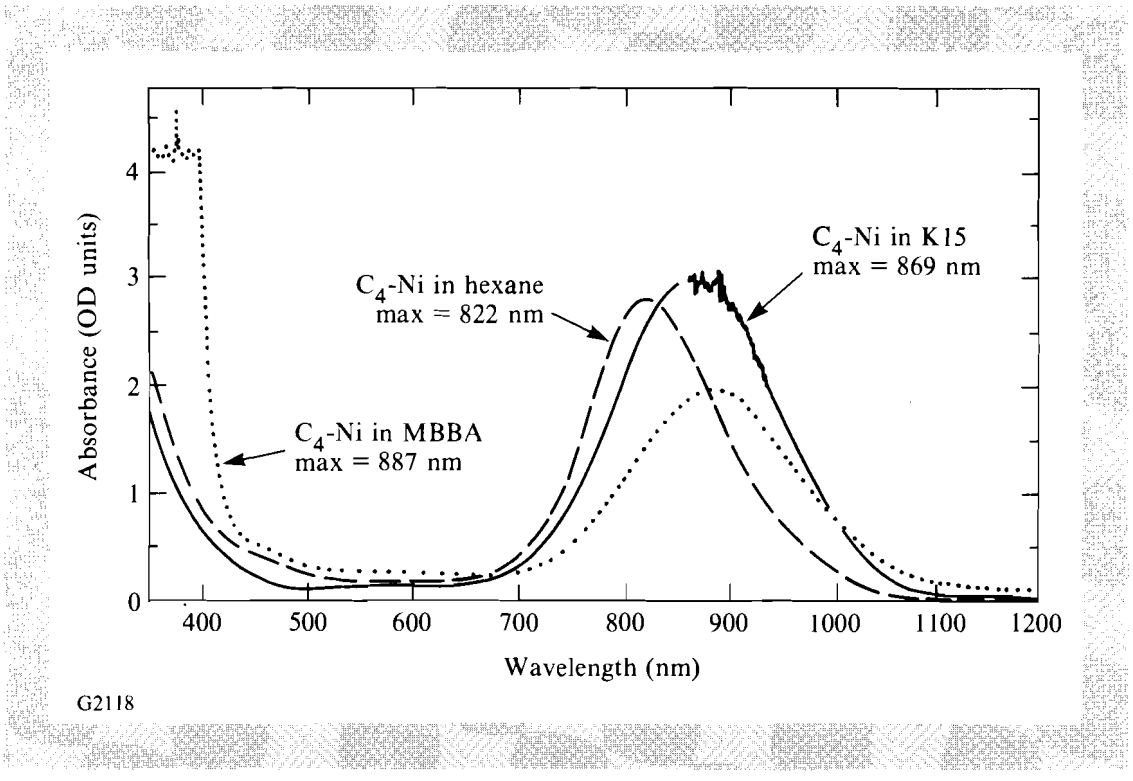

Fig. 33.27
Effect of the solvent matrix on the position of the near-infrared absorption maximum of C_4-Ni. The curve for the complex in hexane was determined in a 1-cm path length for a 50-ppm solution; the curves for K15 and MBBA were determined in 100-μm paths for 0.5% wt/wt of the complex in mixtures held in the isotropic state (50°C).

nematic hosts are shown in Figs. 33.28(a) and 33.28(b). An optical density of 3 is readily obtainable in either host material for a concentration of 0.5%–1% wt/wt and a cell path length of 100 μm. The high solubility of C_4-Ni in the nematic hosts would allow equivalent blocking extinctions to be obtained for thinner path lengths by increasing the concentration of metal complex in the mixtures. A decrease in absorbance with time at 860 nm is observed for a 0.5% solution of the C_4-Ni complex in K15 [Fig. 33.28(a)], indicating that

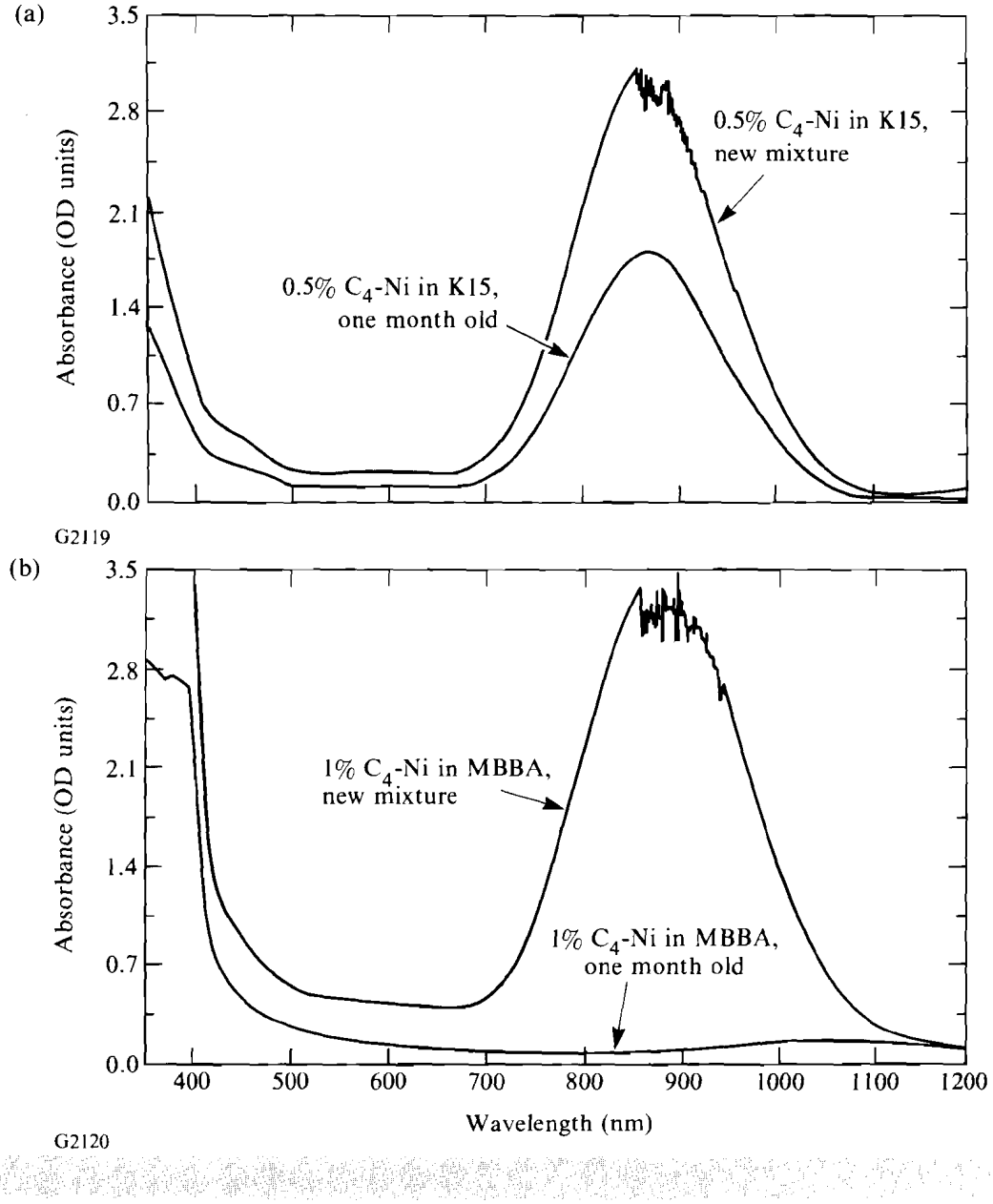

Fig. 33.28
Change in absorbance of mixtures of C_4-Ni in K15 and MBBA after storage for one month. The spectra are for 100-μm path lengths at 50°C.

the metal complex may be decomposing slightly even in K15. This slow decomposition could be initiated by the presence of impurities in the metal complex, and, thus, may not be an indication of a lack of stability of the complex itself. The reduction of the photochemical and thermal stability of various liquid-crystal materials due to the presence of trace impurities is well known and has been extensively documented by Yamagishi *et al.*,[19] and more recently by Lackner, Margerum, and Van Ast.[20] The other possible explanation, separation of the dye complex from solution, seems very unlikely since mixtures with higher concentrations of C_4-Ni have not shown any signs of separation. In the case of mixtures of C_4-Ni in MBBA [Fig. 33.28(b)], the absorption band at 860 nm has completely disappeared, and a new band at 1050 nm is observed. The intensity of this new band is greatly pronounced in mixtures containing a high concentration of the nematic metal complex (Fig. 33.29), and, thus, may be a primary absorption band of a new chemical species resulting from the interaction of C_4-Ni and MBBA.

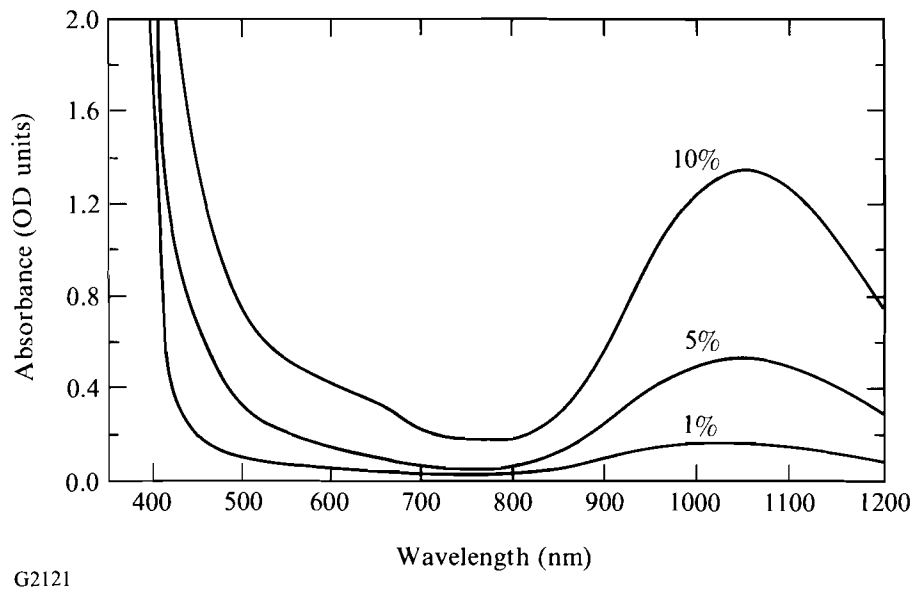

Fig. 33.29
Dependence of the absorbance at 1000 nm–1100 nm on the original metal complex concentration in 100-μm path lengths of one-month-old C_4-Ni/MBBA mixtures. The measurement temperature was 50°C.

The importance of good dye solubility in the liquid-crystal matrix for device applications, such as passive blocking filters or guest-host shutters or modulators, becomes readily apparent upon comparison of the relative blocking efficiencies of C_4-Ni and DMADB-Ni in K15 at their respective peak maxima. The absorption curve for a fresh mixture of 0.5% C_4-Ni in K15, shown in Fig. 33.28(a), is plotted in Fig. 33.30 against the absorption spectrum of the maximum stable concentration of DMADB-Ni (0.05%) in the same host for an equivalent path length. Although the two metal complexes possess similar molar extinction coefficients ($\sim$30,000), the poor solubility of

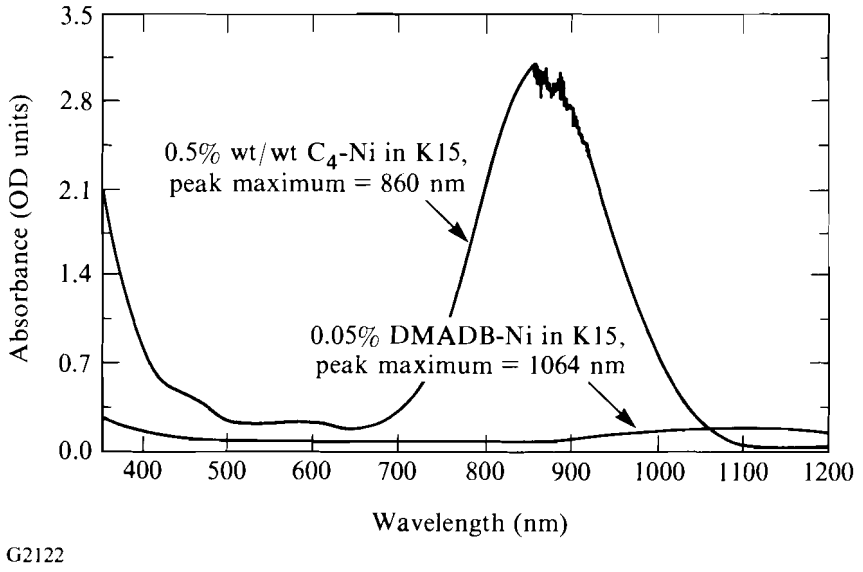

Fig. 33.30
Comparison of the absorption at their respective peak maxima for mixtures of C_4-Ni (0.5% wt/wt) in K15 and DMADB-Ni (0.05% wt/wt) in K15 for 100-μm path lengths.

DMADB-Ni in K15 and the resulting weak absorbance renders this material essentially useless for applications in a liquid-crystal matrix at its peak maximum of 1064 nm.

3. Dichroism and Order Parameter

The positive dichroism in the near-infrared absorption band of C_4-Ni is shown in the absorbance spectra in Fig. 33.31. The measurements were conducted using a 24-μm-thick, homogeneously aligned sample containing 1% wt/wt of C_4-Ni in K15. No difficulty was encountered in producing high-quality homogeneous alignment at this concentration level. A high-frequency ac field (100 KHz) was used to switch the cell to reduce the mixture conductance that occurred at lower frequencies and interfered with the measurements. The maximum transmission was obtained with a 10-V applied field, although switching was observed with fields slightly less than 2 V. The dichroic, or contrast, ratio for C_4-Ni was calculated using corrected absorbance values at 860 nm obtained from the spectra in Fig. 33.31 for the parallel and perpendicular orientations of the metal complex according to the equation:[6]

$$\mathrm{CR} = \frac{A_{\parallel}}{A_{\perp}} = 2.43/0.488 = 4.97 \quad (1)$$

The percent transmission values for the parallel and perpendicular alignment states were 0.29% and 31.8%, respectively. The order parameter S for C_4-Ni in K15 was calculated using the above absorbance values from the expression[6]

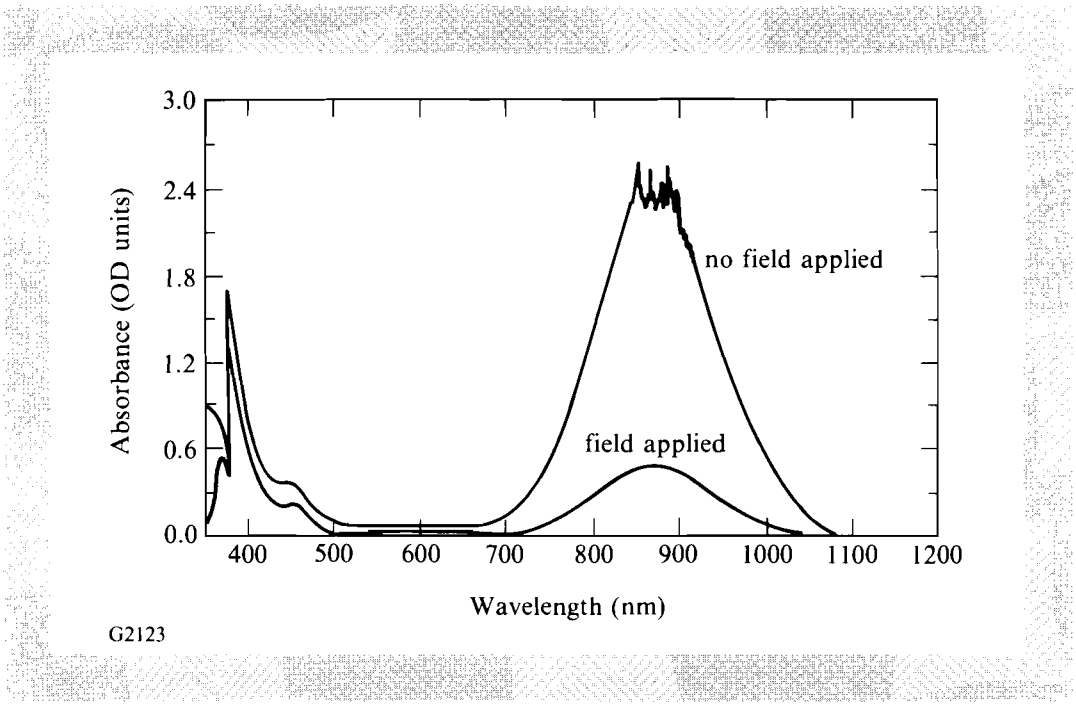

Fig. 33.31
Dichroism of the near-infrared absorption band of C_4-Ni, as measured in a homogeneously aligned, 24-μm-thick cell containing a 1% wt/wt mixture of the complex in K15. Switching between the homogeneous and homeotropic orientations was accomplished with a 10-V, 100-KHz ac field.

$$S = \frac{A_{\parallel} - A_{\perp}}{A_{\parallel} + 2A_{\perp}} \quad . \tag{2}$$

A value for S in K15 of 0.57 was obtained, which is very near the reported maximum range of 0.6–0.8 for S in a nematic liquid crystal.[21] Both the order parameter and dichroic ratio compare favorably to those reported for conventional guest-host dyes for visible region applications.[3–7] To our knowledge, this is the first reported measurement of near-infrared dichroism for a transition metal complex in a nematic host.

Conclusion

The potential of the nematic metal complex bis(*p*-*n*-butylstyryl-1,2-dithiolato)nickel as a near-infrared dichroic dye for use in active and passive liquid-crystal devices for lasers operating near 800 nm has been demonstrated. The high solubility, large optical extinction coefficient, and wide mesomorphic range of these materials are valuable assets in the construction of such devices. Several issues, however, remain to be resolved. The purity of the nematic metal complex may have an effect on its stability in mixtures, and should be more thoroughly investigated. Purification techniques such as preparative high-performance liquid chromatography may be useful for producing samples of well-defined purity. A more rigorous investigation of the solubility of C_4-Ni in K15 and other nematic liquid crystals needs to be undertaken in order to determine the most effective concentration and temperature ranges of mixtures for device applications. The effect of metal complex concentration on the electro-

optic threshold, response time, and dielectric anisotropy of the doped host mixture should also be investigated. The isolation and identification of the species responsible for the 1050-nm peak in aged mixtures of C_4-Ni in MBBA would be of great interest and is currently being investigated. Finally, complexes of other transition metals, such as platinum, palladium, or copper, with ligands of different molecular structures should be prepared and characterized to obtain additional highly soluble dichroic mesogens for applications involving near-infrared laser sources at longer wavelengths.

ACKNOWLEDGMENT

This work was supported by the U.S. Department of Energy Office of Inertial Fusion under agreement No. DE-FC08-85DP40200 and by the Laser Fusion Feasibility Project at the Laboratory for Laser Energetics, which has the following sponsors: Empire State Electric Energy Research Corporation, New York State Energy Research and Development Authority, Ontario Hydro, and the University of Rochester. This work was also supported in part by the Pacific Sierra Research Corporation and the Army Research Office. Such support does not imply endorsement of the content by any of the above parties.

REFERENCES

1. J. K. Foitzik and W. Haase, *Mol. Cryst. Liq. Cryst. (Letters)* **82**, 131 (1982).
2. R. E. Sah, *Mol. Cryst. Liq. Cryst.* **129**, 315 (1985).
3. S. Imazeki, A. Mukoh, T. Yoneyama, and M. Kaneko, *Mol. Cryst. Liq. Cryst.* **145**, 79 (1987).
4. A. V. Ivashchenko, O. S. Petrova, and V.V. Titov, *Mol. Cryst. Liq. Cryst.* **145**, 25 (1987).
5. Z. Salamon and D. Bauman, *Mol. Cryst. Liq. Cryst. (Letters)* **82**, 115 (1982).
6. A. Bloom and E. B. Priestley, *IEEE Trans. Electron Devices* **ED-24**, 823 (1977).
7. J. Constant *et al.*, *Electron. Lett.* **12**, 514 (1976).
8. N. N. Alekseev *et al.*, *Sov. J. Quantum Electron.* **15**, 1431 (1985).
9. G. N. Schrauzer, *Acc. Chem. Res.* **2**, 72 (1969).
10. K. Ohta *et al.*, *J. Chem. Soc., Chem. Commun.*, 883 (1986).
11. A. M. Giroud, A. Nazzal, and U. T. Mueller-Westerhoff, *Mol. Cryst. Liq. Cryst. (Letters)* **56**, 225 (1980).
12. M. Cotrait *et al.*, *Acta Crystallogr.* **C39**, 833 (1983).
13. U. T. Mueller-Westerhoff, A. Nazzal, R. J. Cox, and A. M. Giroud, *J. Chem. Soc., Chem. Commun.*, 497 (1980).
14. A. M. Giroud, *Ann. Phys.* **3**, 147 (1978).
15. A. M. Giroud and U. T. Mueller-Westerhoff, *Mol. Cryst. Liq. Cryst. (Letters)* **41**, 11 (1977).
16. U. T. Mueller-Westerhoff, A. Nazzal, R. J. Cox, and A. M. Giroud, *Mol. Cryst. Liq. Cryst. (Letters)* **56**, 249 (1980).

17. A. M. Giroud, Organometallic complexes forming liquid crystals. Demande De Brevet D'Invention No. 77, 17667.

18. G. N. Schrauzer and H. N. Rabinowitz, *J. Amer. Chem. Soc.* **90**, 4297 (1968).

19. F. G. Yamagishi, D. S. Smythe, L. J. Miller, and J. D. Margerum, *Liquid Crystals & Ordered Fluids, Vol. 3,* edited by J. F. Johnson and R. S. Porter (Plenum Press, New York, 1978), pp. 475–496.

20. A. M. Lackner, J. D. Margerum, and C. Van Ast, *Mol. Cryst. Liq. Cryst.* **141**. 289 (1986).

21. L. M. Blinov, *Electro-Optical and Magneto-Optical Properties of Liquid Crystals* (Wiley, New York, 1983), p. 19.

Section 3
NATIONAL LASER USERS FACILITY NEWS

National Laser Users Facility (NLUF) activity during the first quarter of FY88 consisted of taking OMEGA target shots for four groups. Experimental data were taken for **J. S. DeGroot** (University of California, Davis), **C. F. Hooper** (University of Florida), **U. Feldman** (Naval Research Laboratory), and **P. Goldstone** (Los Alamos National Laboratory). In addition, proposals for FY89 were accepted.

Thirteen OMEGA target shots were taken for J. S. DeGroot's NLUF experiment during the first two weeks of October. High-intensity ($>10^{16}$ W/cm^2) irradiation of CH spheres was used to study ion-acoustic decay instabilities in the corona of the plasma. This experiment is being done in collaboration with **W. Seka** (LLE). These initial shots pointed out improvements needed in the diagnostic instrumentation. Further shots on OMEGA will be scheduled as time becomes available.

Eighteen OMEGA target shots were taken for C. F. Hooper. **M. C. Richardson** (LLE) is collaborating with Prof. Hooper to study x-ray line emission from dense Ar and Ar-Kr plasmas. Plastic microballoons were filled with varying pressures of Ar and Ar-Kr mixtures and then imploded with the OMEGA laser. Time-dependent and time-integrated x-ray spectra were collected for these targets. The data are being analyzed at the University of Florida and LLE to understand the line emission from a dense plasma.

U. Feldman took four OMEGA target shots on spherical targets with layers of Pr, Gd, and Dy. The objective of these shots was to study Na-like line emission from atoms with Z's between 59 and 69. The NRL-NASA 3-m grazing-incidence spectrograph was used to collect XUV spectra from these targets.

A group of scientists from LANL led by P. Goldstone took 58 OMEGA target shots to measure the efficiency of converting absorbed laser energy into x-ray energy. Targets with layers of Ta, Au, Bi, and U were used to study x-ray conversion efficiency as a function of incident intensity. All available x-ray instrumentation on the OMEGA target chamber was used to measure the spectra and time dependence of x rays emitted by these high-Z targets.

Proposals for experiments to be done in FY89 were due to the NLUF manager by 15 December. These proposals will be reviewed by the steering committee during the second quarter of FY88 and principal investigators will be notified by the end of that fiscal quarter.

For more information regarding proposal guidelines and the resources available at the National Laser Users Facility, please contact

Manager
National Laser Users Facility
Laboratory for Laser Energetics
University of Rochester
250 East River Road
Rochester, New York 14623-1299
(716) 275-2074

ACKNOWLEDGMENT

This work was supported by the U.S. Department of Energy Office of Inertial Fusion under agreement No. DE-FC08-85DP40200.

Section 4
LASER SYSTEM REPORT

4.A GDL Facility Report

GDL continued operations this quarter as a target interaction facility. Campaigns executed with the GDL laser included several shots for the x-ray laser program, x-ray microscopy experiments, and laser-target interaction physics experiments. Highlights of the period include a return of the active mirrors to service in GDL, and a return to second- and third-harmonic operation of GDL.

A summary of GDL activities for this quarter follows:

Target Shots	52
Beamline Tests and Alignment	215
Active Mirror Tests	122
TOTAL	389

4.B OMEGA Facility Report

The OMEGA laser system saw extensive service as a target interaction facility during this quarter. The Laboratory continued its efforts to achieve the milestone of 100 times liquid density in deuterium-tritium target implosions. Interposed among the high density experiments were a large number of experiments by the University of Florida (argon-filled polymer-shell implosions) and Los Alamos National Laboratory

(x-ray conversion measurements), under the auspices of the National Laser Users Facility.

During this quarter, the cryogenic target positioner was removed from service and retrofitted with a linear motor for cooling shroud retraction. A series of shots on noncyrogenic DT targets was also taken to verify the knock-on diagnostic performance. In addition, shots were taken to test various uniformity improvements, which included improved energy measurement calibration, more accurate transport optics measurements, distributed phase plates, and better focusing techniques.

A summary of OMEGA operations for this quarter follows:

Target Shots	232
Driver Shots and Tests	98
Beamline Tests and Alignment Shots	162
TOTAL	492

With 232 target shots this quarter, the total number of target shots in calendar year 1987 was 982.

ACKNOWLEDGMENT

This work was supported by the U.S. Department of Energy Office of Inertial Fusion under agreement No. DE-FC08-85DP40200 and by the Laser Fusion Feasibility Project at the Laboratory for Laser Energetics, which has the following sponsors: Empire State Electric Energy Research Corporation, New York State Energy Research and Development Authority, Ontario Hydro, and the University of Rochester. Such support does not imply endorsement of the content by any of the above parties.

PUBLICATIONS AND CONFERENCE PRESENTATIONS

Publications

T. Jackson, J. Nees, R. Vallee, and G. Mourou, "Novel Method for Ultrahigh-Frequency Electro-Optic Time-Domain Reflectometry," *Electron. Lett.* **23**, 1130–1131 (1987).

R. W. Short, W. Seka, and R. Bahr, "Stimulated Raman Scattering in Self-Focused Light Filaments in Laser-Produced Plasmas," *Phys. Fluids* **30**, 3245–3251 (1987).

J. Delettrez, R. Epstein, M. C. Richardson, P. A. Jaanimagi, and B. L. Henke, "Effect of Laser Illumination Nonuniformity on the Analysis of Time-Resolved X-Ray Measurements in UV Spherical Transport Experiments," *Phys. Rev. A* **36**, 3926–3934 (1987).

T. Y. Hsiang, J. F. Whitaker, R. Sobolewski, D. R. Dykaar, and G. A. Mourou, "Propagation Characteristics of Picosecond Electrical Transients on Coplanar Striplines," *Appl. Phys. Lett.* **51**, 1551–1553 (1987).

J. H. Kelly, D. L. Smith, J. C. Lee, S. D. Jacobs, D. J. Smith, J. C. Lambropoulos, and M. J. Shoup III, "High-Repetition-Rate Cr:Nd:GSGG Active-Mirror Amplifier," *Opt. Lett.* **12**, 996–998 (1987).

S. Skupsky, " 'Coulomb Logarithm' for Inverse-Bremsstrahlung Laser Absorption," *Phys. Rev. A* **36**, 5701–5712 (1987).

B. Yaakobi, "X-Ray Lasers: A Progress Report," *Photonics* **21**, 65 (1987).

R. L. McCrory, J. M. Soures, P. Audebert, O. Barnouin, R. S. Craxton, J. Delettrez, R. Epstein, L. Forsley, R. J. Hutchison, P. Jaanimagi, S. Jacobs, R. L. Keck, T. Kessler, H. Kim, R. Kremens, S. A. Letzring, R. S. Marjoribanks, F. Marshall, P. McKenty, G. A. Mourou, M. C. Richardson, W. Seka, R. W. Short, A. Simon, S. Skupsky, C. Verdon, J. Wark, B. Yaakobi, S. E. Bodner, J. P. Dahlburg, M. Emery, J. Gerdner, J. Grun, T. Lee, C. Manka, E. McLean, S. Obenschain, B. Ripin, and J. Stamper, "Direct-Drive Laser Fusion in the United States of America," *Plasma Physics and Controlled Nuclear Fusion Research 1986* (International Atomic Energy Agency, Vienna, 1987), Vol. 3, pp. 47–54.

J. F. Whitaker, R. Sobolewski, D. R. Dykaar, T. Y. Hsiang, and G. A. Mourou, "Subpicosecond Pulse Propagation on Superconducting Striplines," *Proceedings of the 18th International Conference on Low Temperature Physics*, Kyoto, Japan, 1987; *ibid.*, *Japanese Journal of Applied Physics* **26**, Supplement 26-3 (1987).

J. C. Lee, S. D. Jacobs, and A. Schmid, "Retro-Self-Focusing and Pinholing Effect in a Cholesteric Liquid Crystal," *Mol. Cryst. Liq. Cryst.* **150b**, 617–629 (1987).

J. Nees and S. Williamson, "A Technique for Wing Suppressed IR Sampling," in *Picosecond Electronics and Optoelectronics II*, edited by F. J. Leonberger, C. H. Lee, F. Capasso, and H. Morkoc (Springer-Verlag, Berlin, Heidelberg, New York, London, Paris, Tokyo, 1987), pp. 33–35; G. Mourou, K. Meyer, J. Whitaker, M. Pessot, R. Grondin, and C. Caruso, "Ultrafast Optics Applied to Modern Device Research," *ibid.*, pp. 40–48; R. Sobolewski, D. R. Dykaar, T. Y. Hsiang, and G. A. Mourou, "Picosecond Switching in Josephson Tunnel Junctions," *ibid.*, pp. 177–180; W. R. Donaldson, "High-Speed, High-Repetition-Rate, High-Voltage Photoconductive Switching," *ibid.*, pp. 241–244.

J. C. Moreno, S. Goldsmith, H. R. Griem, L. Cohen, and M. C. Richardson, "Identification of New Ti XXI and Ti XIX Transitions Emitted by Laser-Produced Plasmas," *J. Opt. Soc. Am. B* **4**, 1931–1933 (1987).

Forthcoming Publications

The following papers are to be published in the *Proceedings of the 17th Annual Boulder Damage Symposium*, Boulder, CO, October 1985:

K. A. Cerqua, S. D. Jacobs, B. L. McIntyre, and W. Zhong, "Ion Exchange Strengthening of Nd-Doped Phosphate Laser Glass."

B. Liao, D. J. Smith, and B. L. McIntyre, "The Development of Nodular Defects in Optical Coatings."

D. J. Smith, B. Krakauer, C. J. Hayden, A. W. Schmid, and M. J. Guardalben, "Yttrium-Oxide-Based Anti-Reflection Coating for High Power Lasers at 351 nm."

B. Yaakobi, "X-Ray Diagnostic Methods for Laser-Imploded Targets" and "Thermal Transport, Mass Ablation, and Preheat in Laser-Target Experiments," to be published in the *Proceedings of the Spring College on Radiation in Plasmas,* Trieste, Italy, June 1985 (World Scientific Publishing Co.).

G. Mourou, "Picosecond Electro-Optic Sampling," to be published in the *Proceedings of the High Speed Electronics Conference*, Stockholm, Sweden, August 1986.

R. L. McCrory and J. M. Soures, "Inertially Confined Fusion," to be published in *Applications of Laser Plasmas,* Chapter 7.

K. A. Cerqua, J. Hayden, and W. C. LaCourse, "Stress Measurements in SOL-GEL Films," to be published in the *Journal of Non-Crystalline Solids*.

J. F. Whitaker, R. Sobolewski, D. R. Dykaar, T. Y. Hsiang, and G. A. Mourou, "Propagation Model for Ultrafast Signals on Superconducting Dispersive Striplines," to be published in a special issue of *IEEE Transactions on Microwave Theory and Techniques.*

P. Maine, D. Strickland, P. Bado, M. Pessot, and G. Mourou, "Generation of Ultrahigh-Peak-Power Pulses by Chirped Pulse Amplification," to be published in the *IEEE Journal of Quantum Electronics*.

W. Watson, "Vacuum-Assisted Contaminated Particulate Removal," to be published in the *Journal of Vacuum Science and Technology*.

A. Simon and R. W. Short, "Comments on 'Motion of an Electron Bunch Through a Plasma'," to be published in *Physics of Fluids*.

H. E. Elsayed-Ali and G. A. Mourou, "Picosecond Reflection High-Energy Electron Diffraction," to be published in *Applied Physics Letters*.

P. C. Cheng, H. G. Kim, D. M. Shinozaki, K. H. Tan, and M. D. Wittman, "X-Ray Microscopy—Its Application to Biological Sciences," to be published in the *Proceedings of the X-Ray Microscopy Meeting '87,* Stony Brook, NY, September 1987 (Springer-Verlag).

K. L. Marshall and S. D. Jacobs, "Near-Infrared Dichroism of a Mesogenic Transition Metal Complex and Its Solubility in Nematic Hosts," to be published in *Molecular Crystals and Liquid Crystals.*

Conference Presentations

The following presentations were made at Atomic Processes in Plasmas, Santa Fe, NM, 28 September–2 October 1987:

P. Audebert, T. Boehly, M. Russotto, D. Shvarts, J. M. Soures, and B. Yaakobi, "A Measurement of Counterstreaming Between Two Exploding-Foil Plasmas."

T. Boehly, D. Shvarts, P. Audebert, D. Bradley, R. S. Craxton, R. Epstein, M. Russotto, J. M. Soures, and B. Yaakobi, "X-Ray Laser Studies at LLE."

H. Kim, "Parylene Ablation Layer Coating of Mechanically Non-Supported Inertial Fusion Targets," presented at the JOWOG 28A Workshop on Organic Coatings, LANL, Los Alamos, NM, 6–8 October 1987.

T. Kessler, D. Smith, N. Sampat, S. Swales, W. Castle, and M. Wohl, "Thin Film Distributed Phase Plates," presented at the Optical Society of America Annual Meeting and Workshop on Optical Fabrication and Testing, Rochester, NY, 20–23 October 1987.

The following presentations were made at the 8th International Workshop on Laser Interaction and Related Plasma Phenomena, Monterey, CA 26–30 October 1987:

R. L. McCrory, "Ultra-High Pressure Ablative Compression Experiments on OMEGA" (invited paper).

M. C. Richardson, "High-Density Implosion Diagnostics."

The following presentations were made at the American Physical Society Conference, San Diego, CA, 30 October–6 November 1987:

S. H. Batha, R. Bahr, L. M. Goldman, W. Seka, and A. Simon, "Observations of Enhanced Thomson Scattering."

T. Boehly, P. Audebert, B. Boswell, D. Bradley, R. S. Craxton, R. Epstein, M. C. Richardson, M. Russotto, D. Shvarts, J. M. Soures, and B. Yaakobi, "X-Ray Laser Studies at LLE."

B. Boswell, D. Shvarts, T. Boehly, and B. Yaakobi, "Effects of Refraction on Beam Propagation and Amplification in Various X-Ray Laser Geometries."

R. S. Craxton, W. Seka, and C. Gomez, "Computer Simulations of a Self-Focusing Experiment under Reactor-Like Conditions."

J. Delettrez, D. Bradley, R. Epstein, P. Jaanimagi, M. C. Richardson, and S. Skupsky, "Effects of Illumination Nonuniformity on the Interpretation of X-Ray Diagnostics in Glass Microballoon Implosions."

E. M. Epperlein, "2-D Nonlocal Electron Thermal Transport in Laser-Produced Plasmas."

R. Epstein, D. Shvarts, S. Skupsky, and B. Yaakobi, "The Design and Optimization of Recombination X-Ray Lasers."

L. M. Goldman, "Areal Density and Mix Measurement in IF Plasmas."

F. J. Marshall, S. Letzring, C. P. Verdon, R. Keck, H. Kim, J. Knauer, R. Kremens, S. Noyes, G. Pien, M. C. Richardson, F. Rister, M. Wittman, R. L. McCrory, and J. M. Soures, "Cryogenic Target Experiments on the OMEGA Laser."

P. W. McKenty, S. Skupsky, C. P. Verdon, and R. L. McCrory, "Evaluation of Time-Dependent Illumination Uniformity Patterns of Imploding Laser Fusion Targets."

S. Radin, R. W. Short, and A. Simon, "Long Time Simulations of the Single-Mode, Bump-on-Tail Instability."

M. C. Richardson, P. Audebert, D. Bradley, J. Delettrez, P. A. Jaanimagi, R. Keck, R. Kremens, F. J. Marshall, R. L. McCrory, P. W. McKenty, J. M. Soures, and C. P. Verdon, "High-Density, Gas-Filled Target Implosions."

W. Seka, T. Kessler, F. J. Marshall, M. C. Richardson, J. M. Soures, and R. Bahr, "Target Irradiation Uniformity Experiments with Spatial Phase Scramblers."

R. W. Short, "Self-Focusing of Hot Spots in Multiple-Beam Illumination Geometries."

A. Simon, R. W. Short, W. Seka, and L. M. Goldman, "Alternative Analysis of CO_2 Laser-Produced Plasma Waves."

S. Skupsky and T. Kessler, "A Source of Hot Spots in Frequency-Tripled Laser Light."

P. A. Jaanimagi, D. K. Bradley, J. Delettrez, C. Hestdalen, P. W. McKenty, M. C. Richardson, and C. P. Verdon, "Time-Resolved X-Ray Imaging of ICF Implosions."

S. A. Letzring, F. J. Marshall, R. Kremens, R. L. McCrory, G. Pien, J. M. Soures, C. P. Verdon, M. Wittman, R. Gram, T. Kessler, F. Rister, C. Hestdalen, D. Musinski, D. Dekker, M. Mruzek, J. Ankney, and W. J. Filmlee, "Design of and Initial Target Experiments with a Cryogenic Target Positioning System for the 24-Beam OMEGA System."

C. P. Verdon, "Hydrodynamic Stability of Ablatively Driven Pellet Implosions" (invited paper).

N. Sampat and S. Swales, "Issues in Image Processing Software Development for a Multiuser, Multiprogramming Environment," presented at Electronic Imaging '87, World Trade Center, Boston, MA, 2–5 November 1987.

R. Q. Gram, C. K. Immesoete, H. Kim, and L. Forsley, "Bounce-Coated Ablation Layers on Fusion Targets," presented at the American Vacuum Society's 34th National Symposium and Topical Conference, Anaheim, CA, 2–6 November 1987.

The following presentations were made at the American Chemical Society's 17th Northeast Regional Meeting, Rochester, NY 8–11 November 1987:

Y. F. Maa, S. H. Chen, and K. L. Marshall, "Chemical Modification of Polymeric Nucleophiles."

M. L. Tsai, S. H. Chen, and K. L. Marshall, "Liquid Crystalline Side-Chain Copolymers Exhibiting the Cholesteric Phase."

S. D. Jacobs, K. J. Skerrett, S. F. B. Morse, R. J. Hutchison, A. Schmid, K. L. Marshall, K. A. Cerqua, M. J. Guardalben, and T. J. Kessler, "Performance of the Frequency-Tripled OMEGA High-

Peak-Power Nd:Glass Laser System with Liquid-Crystal Polarizers," presented at the 1987 International Conference on Lasers, Xiamen (Amoy), China, 15–19 November 1987.

The following presentations were made at the Winter Meeting of the Materials Research Society, Boston, MA, 1–6 December 1987:

J. C. Lambropoulos, "Analysis of Thermal Stresses, Fracture, and Strengthening in Optical Glass for High-Average-Power Lasers."

J. C. Lambropoulos and B. Wilner, "The Effect of Laser-Induced Damage of Thermal and Mechanical Properties of Optical Materials in Thin Film Form."

The following presentations were made at the Laser '87 Conference, Lake Tahoe, NV, 7–11 December 1987:

G. Ball, W. Seka, and S. Letzring, "Injection-Seeded Nd:YLF Q-Switched Laser."

J. F. Seely, U. Feldman, C. M. Brown, W. E. Behring, and M. C. Richardson, "High-Resolution XUV Spectroscopy Using the OMEGA Laser" (invited talk).

G. Mourou, "High-Speed Circuit Testing Using Ultrafast Optical Techniques," presented at the First European Conference on Electron and Optical Beam Testing of Integrated Circuits, Grenoble, France, 9–11 December 1987.

J. F. Whitaker, G. A. Mourou, and K. A. Bhasin, "Millimeter Wave MMIC Characterization by Noncontact Electro-Optic Sampling," presented at the 12th International Conference on Infrared and Millimeter Waves, Grosvenor Resort, FL, 14–18 December 1987.

ACKNOWLEDGMENT

The work described in this volume includes current research at the Laboratory for Laser Energetics, which is supported by Empire State Electric Energy Research Corporation, New York State Energy Research and Development Authority, Ontario Hydro, the University of Rochester, and the U.S. Department of Energy Office of Inertial Fusion under agreement No. DE-FC08-85DP40200.